ABSTRACT

JOSHI, PRATIK. High-Temperature Deformation Characteristics of Cladding Materials for Nuclear Reactors: HANA-4 and FeCrAl. (Under the direction of Dr. KL Murty).

Zr-Nb alloys are used as cladding materials to encapsulate radioactive fuel in nuclear reactors. They possess excellent corrosion resistance at high temperatures making it possible to achieve high fuel burn-up directly increasing the thermal efficiency of the reactor. While they are commonly used in recrystallized (Rx) form in boiling water reactors, there is a need to understand the effect of cold work and stress relief (CWSR) on biaxial creep characteristics of these materials due to their use in pressurized water reactor during operation, these alloys experience multiaxial loading conditions. In this study, the biaxial creep behavior of as-received Zr-Nb alloy commonly referred to as HANA-4 has been investigated at 500 °C. The crystallographic textures and creep loci of the as-received HANA-4 have been evaluated. Later, these have been compared with the previous study done on recrystallized HANA-4. Biaxial creep tests were performed using internally pressurized tubing superimposed with the axial load under varied hoop (σ_θ) to axial (σ_z) stress ratios of 0 to 2 while monitoring both the axial and hoop strains using an LVDT and a laser telemetric extensometer respectively. The creep loci of HANA-4 was found to be not greatly affected by initial state (CWSR or Rx) and R&P values were evaluated to be 1.5 and 0.95 respectively. The simulated creep loci using crystallite orientation distribution functions (CODFs) showed excellent agreement with experimental results.

The Loss of Coolant Accident (LOCA) at Fukushima Daichi nuclear reactor in 2011, has attracted attention toward the development of new cladding materials with improved performance in the beyond-design-basis-accidents scenario. In this context, FeCrAl shows better oxidation resistance compared to Zircaloy especially at temperatures greater than 1200 °C. However, creep deformation behavior of FeCrAl base alloys are largely unknown. In this study, the burst tests of

Fe-12wt%Cr-6Al-0.05Y (C26M2) alloy in the temperature range of 480-600 °C were carried out at a wide range of hoop stresses. From this study, the values of stress exponents (n) for creep and activation energy (Q_C) were evaluated to be 5.1 ± 0.5 and 289 ± 25 kJ/mol respectively. The obtained results suggest dislocation climb as the main creep mechanism.

High-Temperature Deformation Characteristics of Cladding Materials for Nuclear Reactors: HANA-4 and FeCrAl

by
Pratik Joshi

A thesis submitted to the Graduate Faculty of
North Carolina State University
in partial fulfillment of the
requirements for the degree of
Master of Science

Nuclear Engineering

Raleigh, North Carolina
2019

APPROVED BY:

_____	_____
Dr. KL Murty Committee Chair	Dr. Ron Scattergood
_____	_____
Dr. Mohammad Bourham	Dr. Ge Yang

DEDICATION

This thesis is dedicated to all my teachers and mentors.

BIOGRAPHY

Pratik Prasanna Joshi was born in Nashik, India on January 15, 1996, to his parents, Prasanna Joshi and Rujuta Joshi. He did his schooling and engineering in Pune, India. During his high school years, an interest surfaced in chemistry and physics. Materials Science required the knowledge of both chemistry and physics, this made him interested to join the Dept. of Materials science and Engineering at College of Engineering, Pune (COEP), the 3rd oldest college in Asia. Soon he was fascinated by the science of metals especially physical metallurgy of steels. He was also awarded the steel scholarship by Ministry of Steel, Govt of India for excellent academic performance during his last two years of engineering. Since, most of the components in the nuclear industry such as reactor pressure vessel (Low Carbon Steel), Fuel cladding (Zirconium), Structural materials (Austenitic Stainless Steels, Ni-based alloys), etc are made up of metals which aligned with his interests, after his graduation in May 2017 he decided to join the Master's Program in the Nuclear Engineering Department at NC State University and work on Nuclear Materials with Dr. KL Murty's research group.

ACKNOWLEDGEMENTS

I am deeply grateful to Dr. K.L. Murty for his constant guidance and support throughout my time at the Nuclear Materials group. He always provided a healthy and conducive atmosphere for learning and research where creativity and innovation was rewarded.

I would like to extend my thankfulness to my committee members Prof. Mohamad Bourham, Prof. Ge Yang and Prof. Ronald Scattergood for their valuable time and thought-provoking critiques.

I would like to thank Dr. Jacob Eapen and Dr. Robert Hayes. I was a teaching assistant for their class and this helped me with my teaching skills and provided me with financial support.

I am very grateful to Dr. Nilesh Kumar, Dr. Abdullah Alomari and Dr. Boopathy Kombiah who acted as my mentors. They helped me hone my experimental skills. I thank Dr. Nedim Cinbiz of ORNL who provided me with the necessary materials, guidance and support when needed.

My thanks are due to Mr. Ervin Miller of Nuclear engineering for helping in solving issues with our instruments to run my experiments smoothly especially the burst testing experiments.

My collegues at the nuclear materials group were special. I would like to thank Leonardi, Zeinab, Micah and Mahmoud. They helped me relax and maintain my calm when somethings didn’t turn out the way they were supposed to be.

I would like to thank Jamison (Undergraduate student) for polishing some of my samples which saved my time and work. Guiding him helped improve my leadership skill.

My stay in Raleigh is one of the best parts in my life thanks to my friends Vikram, Sumit, Nikhil, Pushkar, and Hermab.

No amount of gratitude would be enough to my family back in India for their continuing support.

TABLE OF CONTENTS

LIST OF TABLES

LIST OF FIGURES

CHAPTER 1- THESIS OVERVIEW

1.1. Introduction

Growing cities, rise in population, and the desire for a modern lifestyle has made the use of sophisticated gadgets inevitable. These gadgets demand a great deal of energy giving rise to the fear of an energy crisis. To combat this problem, most countries rely heavily on power from coal and natural gas. This has resulted in increasing CO_2 emissions, responsible for climate change. The issues such as rising air pollution, limited land area, large variations in wind and sunlight make nuclear energy the most attractive option to overcome the shortage of energy in a sustainable way. The major issue faced by nuclear energy is safety during plant operation. This issue can be tackled by continuous innovation in nuclear materials. The presence of severe conditions acting in tandem such as radiation of varying energy, high temperature, highly corrosive environments, and mechanical and thermal stresses make this task challenging.

1.2. Cladding Materials in Nuclear Reactors

The major components of Nuclear reactors are fuel, metal cladding, the reflector, control rods, the moderator, reactor pressure vessel, and structural materials to provide support. The fuel in LWRs is ceramic UO_2 in the form of pellets. These ceramic pellets are enclosed in a metal cladding. The metal cladding should be transparent to neutrons so that these neutrons can cause fission of the UO_2 fuel.

To make nuclear power more competitive and safe there are two major requirements:

1.2.1. High Fuel Burnup

The companies in charge of running these reactors need to burn the maximum amount of fuel in the reactor so as to extract the maximum amount of heat from the fuel. This is referred to

as high fuel burnup. This leads to better plant economics, placing additional demands on fuel cladding most common being high corrosion resistance.

1.2.2. Accident Tolerant Cladding

The release of radioactivity to the environment is a major threat to people's health in case of a nuclear accident. The most critical barrier to the release of radioactivity to the environment is the cladding material. The innovation of materials in the nuclear sector has been rather slow compared to other sectors. The conventional Zircaloys discovered in the 1950s with some modifications are still being used as cladding materials in current generation reactors. Efforts are underway to find and test the alternative cladding materials better than Zircaloy, this has gained momentum after the recent Fukushima accident since, zirconium doesn't show high oxidation resistance above 1200 ^{0}C. The current candidates to replace Zircaloy are FeCrAl, SiC-SiC Composites, and Chromium-coated Zircaloy.

1.3. Motivation

There is a need to understand creep behavior of cladding materials especially those that are designed to have optimum properties during high fuel burnup (Zirconium based HANA-4) and loss of coolant accidents (Iron based FeCrAl) since this data is scarce or doesn't exist.

1.4. Goals

This study has two goals:

a) To generate creep loci of as-received HANA-4 by performing biaxial creep tests and to verify the active slip system by using Crystalline Orientation Distribution function (CODF)
b) To study the creep behavior of newly developed commercial FeCrAl alloys so as to identify the active creep mechanism(s) in the temperature range of 480-600 ^{0} C using burst testing.

1.5. Biaxial Creep behavior of HANA 4

This study involved the following:

1.5.1. Uniaxial and Biaxial Creep Tests of CWSR HANA 4

Creep tests were carried out for different axial stresses and hoop stresses, which produced different stress ratios (0, 0.5, 1, 1.5 and 2) at 500 °C. The purpose of the creep tests was to determine the strain-rate, strain ratios vs stress ratios, the anisotropy parameters (R and P), and to generate the creep loci of as-received HANA-4.

1.5.2. Texture Analysis

Texture measurements were carried out on CWSR HANA 4 tubes. The textures were represented in the forms of inverse pole figures and direct pole figures using Electron Backscattered Diffraction (EBSD).

1.5.3. CODF calculation and plasticity modeling

Crystallite Orientation Distribution Function (CODF) is a quantitative measure of crystallographic texture. Anisotropic parameters (R and P), creep strain-rate ratios vs stress ratios and creep loci were predicted from CODF combined with a lower-bound deformation model.

1.6. Creep Characteristics of FeCrAl

This study involved:

1.6.1. Burst Test of FeCrAl-C26M2 (12% Cr, 6% Al)

FeCrAl tubes were internally pressurized at fixed pressures with Argon gas in the temperature range of 480- 600 ^{0}C and the time to burst was recorded. The purpose was to determine the approximate creep rate which was used to find the operative creep mechanism(s) and the activation energy for creep.

CHAPTER 2- LITERATURE REVIEW

2.1. Fundamentals of Creep

2.1.1. Definition

Creep is time-dependent strain occurring at constant stress (below the yield stress) when the material is subjected to temperatures above 0.4 Tm, where T_m is the absolute melting temperature.

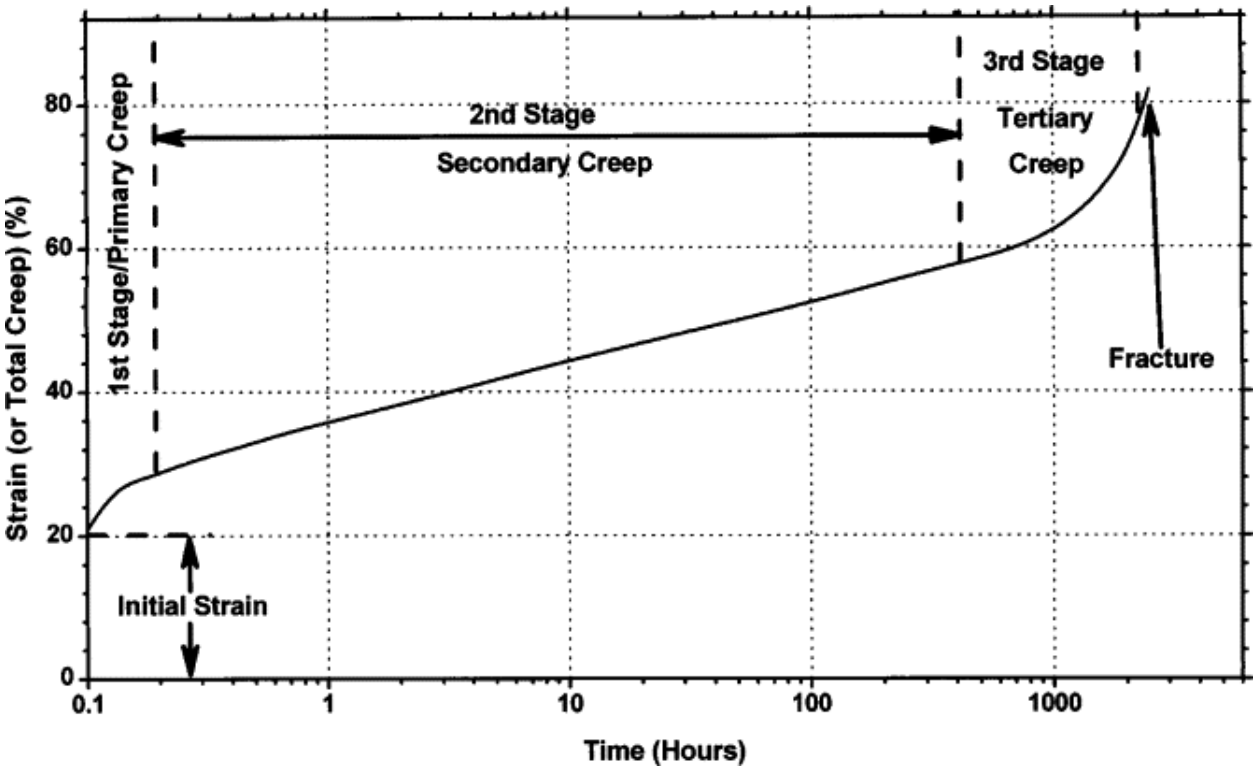

Figure 2.1. Schematic of a typical creep curve [1].

Figure 2 .1 shows a typical creep curve showing 3 distinct stages. 1st stage is the primary creep where strain rate increases with time. 2nd Stage is known as secondary creep, the creep rate is constant with respect to time known as steady-state creep rate sometimes also referred to as minimum creep rate. In the 3rd stage the material fractures known as tertiary creep.

2.1.2. Creep Mechanisms

It has been observed that the factors which affect diffusion also affect creep. Hence, creep is a diffusion controlled process [1]. The basic mechanisms in creep can involve not only dislocation motion but also diffusion of vacancies or atoms. Creep becomes generally more pronounced at high temperatures where diffusion of vacancies is considerably faster. However, some materials can creep even at room temperature or sub-zero temperatures [2]. Creep tests at low normalized stresses and low homologous temperatures are time-consuming since the strain rate can be pretty low. Hence, creep tests are usually carried out at high homologous temperatures and normalized stresses to measure steady-state creep rate in short duration. However, carrying out tests at too high stresses can result in Power Law breakdown (PLB). Additionally, blindly extrapolating these results to low temperature and stresses can lead to erroneous results as there can be transitions in creep mechanisms. A general equation representing the steady-state creep rate controlled by any of the creep mechanisms can be stated as follows in the form of BMD equation [3],

$$\frac{\dot{\varepsilon} k_b T}{DEb} = A\left(\frac{b}{d}\right)^p \left(\frac{\sigma}{E}\right)^n \tag{2.1}$$

where $\dot{\varepsilon}$ is the steady state creep rate, D the diffusion coefficient that characterizes a particular creep mechanism, E the elastic modulus, b the burger's vector, k_b the Boltzmann Constant, T the temperature, d the grain size, σ the applied shear stress, A the pre-factor, p the inverse grain size exponent and n the stress exponent. Table 2.1 shows the values of the constants predicted for various creep mechanisms

Table 2.1. Constants in equation (1.1) for various creep mechanisms [4].

Creep Mechanisms	**A**	**p**	**n**
Coble	100	3	1
Nabarro-Herring	12	2	1
Grain boundary sliding	200	1-2	2
Dislocation glide	6	0	3
Dislocation climb	6×10^7	0	4-7

2.1.2.1. Dislocation glide & climb

The rate controlling mechanism for creep in power-law region can be either dislocation glide or climb depending on the applied stress, temperature and metal class (Class A- alloy class or Class M -pure metal). In general, for class A alloys, dislocation glide becomes slower than climb owing to the interaction of solutes with dislocations and therefore acts as the rate-controlling mechanism. For Class M alloys the opposite is true. Weertman proposed his model to predict the creep rate for glide mechanism. He assumed the dislocation velocity is proportional to the stress acting on them [5].

The average dislocation velocity [6] is given by,

$$\mathrm{v} = A\sigma^2 b^2 L \qquad (2.2)$$

where A is a constant decided by the type of viscous-glide mechanism. If the dislocation source density is assumed to be M and the dislocation line length is taken to be Λ, the creep rate can then be written as,

$$\dot{\varepsilon}_{ss} \; \alpha \; A \, \Lambda \mathrm{M} b \sigma^2 b^2 L \qquad (2.3)$$

Weertman obtained values of Λ and L to be $3L$ and $(2\sigma/(GbM))^{0.5}$

Substituting these values in equation (2.2), the creep rate was derived as [4],

$$\left(\frac{\dot{\varepsilon}_s k_b T}{DEb}\right) = 6\left(\frac{\sigma}{E}\right)^3 \quad (2.6)$$

Dislocation climb is well explained by Weertman pill-box model [7,8]

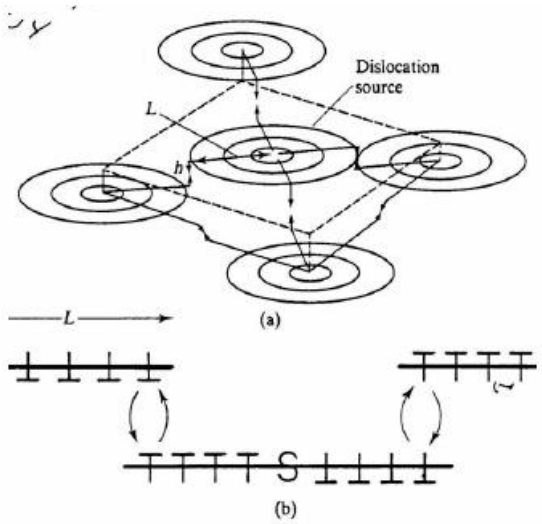

Figure 2.2. Depiction of a) Pill-Box Model b) Dislocation Climb.

This model is referred to as a pill-box model, whose schematic is given in Figure 1.12. In this model, the M number of dislocation sources per unit volume is assumed to be operative. The dislocations generated from the sources glide for a distance of L before climbing up or down to get annihilated with the dislocations approaching in parallel planes. The climbing height is assigned to be h. As seen in Figure 1.12, each dislocation source generates a constant number of dislocation loops on the glide plane. Once the leading dislocation gets annihilated, a dislocation will be released from the source. Based on these initial settings, Weertman has obtained the following relation for the creep rate,

$$\dot{\varepsilon} = \alpha\left(\frac{D_l}{b^{3.5}M^{0.5}}\right)\left(\frac{\sigma}{G}\right)^{4.5}\left(\frac{G\Omega}{k_B T}\right) \quad (2.7)$$

G is the shear modulus, Ω is the atomic volume, is a constant whose values are in the range

0.15 α <0.33, and $Dl = D_0 \exp\left(\frac{-Q_l}{RT}\right)$

2.1.2.2. Grain Boundary Sliding/ Superplastic flow

Grain boundary sliding can also cause plastic deformation under certain conditions. The strain caused by grain boundary sliding is due to the relative motion between the grains resulting from shear stress at the boundaries. This is particularly true at moderate temperatures and low stresses in fine-grained materials [9]. The creep rate obtained by Mukherjee for superplastic flow is as follows [10],

$$\dot{\varepsilon} = 2\left(\frac{D_{gb}Eb}{k_B T}\right)\left(\frac{\sigma}{E}\right)^2\left(\frac{b}{d}\right)^2 \tag{2.8}$$

2.1.2.3. Coble and Nabarro-Herring (N-H) creep

Coble creep and N-H creep are diffusion creep mechanisms. The major difference between the two is N-H creep is volume diffusive whereas coble creep is grain boundary diffusive as shown in figure 2.3. In N-H creep the creep rate is inversely proportional to the square of grain diameter and in Coble the creep rate is inversely proportional to the cube of grain diameter.

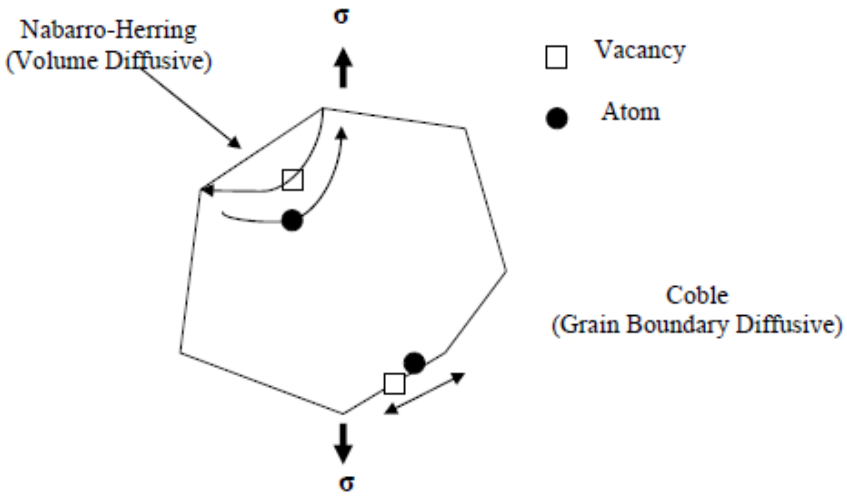

Figure 2.3. Illustration of differences between N-H and Coble creep [7].

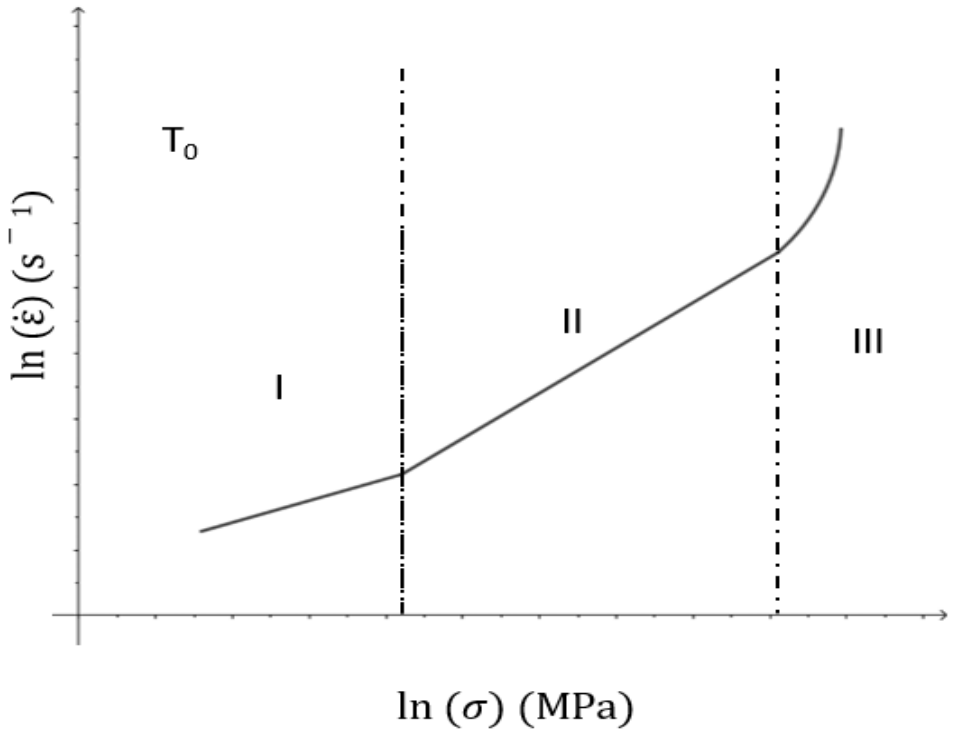

Figure 2.4. General creep behavior of class M alloys.

For Class M alloys in the region I diffusion creep is dominant followed by dislocation climb in region II. PLB takes place at $\left(\frac{\sigma}{E}\right)$>$10^{-3}$ and $\left(\frac{\dot{\varepsilon}}{D}\right)$>$10^{13}$ m^{-2} which is region III. The equation for creep rate used in Power law breakdown is:

$$\frac{\dot{\varepsilon}}{D_L} = A\ exp\left(\frac{B\sigma}{k_B T}\right) \tag{2.9}$$

Where B is related to the activation area for creep.

2.2. Zirconium alloys

2.2.1. Slip systems in Zirconium

The ideal c/a ratio of hcp material is 1.63. Zr has a c/a ratio of 1.593 which is less than the ideal value. The possible slip systems are basal, prismatic and pyramidal as shown in figure 2.3. Slip takes place on the planes that have the highest packing density and the smallest burger's

vector. In short, slip takes place on the planes having the lowest critical resolved shear stress (CRSS). In Zr, the pyramidal slip system has the least Critical Resolved Shear Stress (CRSS) and is dominant [11]. Basal slip has been observed at Room Temperatures, at very high strain rates [12]. Akhtar [13] observed basal slip in pure Zr single crystals above 577^{o}C. At 700^{o}C he reported its CRSS to be ~4 MPa and the CRSS for prismatic slip ~2.5 MPa. In contrast, Wu et al [14] have predicted easy activation of basal slip at room temperature (RT) in Zircaloy-2.

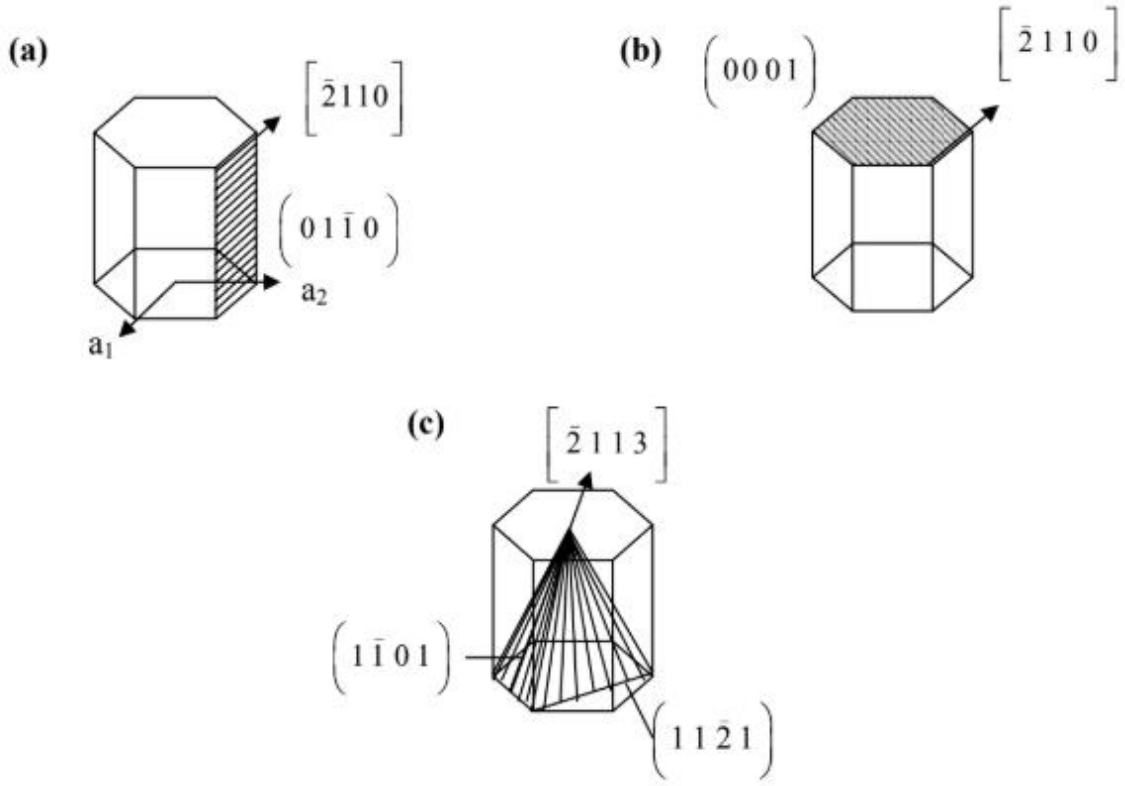

Figure 2.5. Illustration of various slip systems in hcp metals a) prism b) basal c) pyramidal [7].

2.2.2. Nb-modified Zr alloys

Zr-Nb fuel cladding alloys were introduced for high fuel burnup applications. The first departure from Zircaloy-4 in western plants was the introduction of lead assemblies containing ZIRLO® clad fuel in 1987 [15]. Table 2.2 shows the compositions and tradenames of various Zr-Nb alloys. The Russian alloy E110 was used in VVERs (Russian reactors, similar to PWRs). A

second Russian alloy for VVER application was E635, which contained both Sn and Nb [15]. The research and developments of the advanced fuel for a high burn-up was started in 1997 by Korea Atomic Energy Research Institute (KAERI) in collaboration with Korea Nuclear Fuel Company (KNFC) and several universities in order to meet the global demand for an extension of the fuel discharge burn-up to more than 70 GWd/MtU. As a result of the extensive research activities, KAERI had developed six kinds of advanced Zr alloy claddings named HANA (High-performance Alloy for Nuclear Application) [16].

Table 2.2. The composition of various selected Zr-Nb alloys (in wt. %) [17,18].

Materials	**Country of Origin**	**Nb**	**Sn**	**Fe**	**Cr**	**Cu**	**O**
E110	Russia	0.95-1.05	-	0.006-0.012	-	-	≤ 0.1
E110K	Russia	0.95-1.05	-	0.006-0.012	-	-	0.12-0.16
E365	Russia	0.95-1.05	1.1-1.3	0.3-0.4	-	-	0.05-0.12
M5	France/USA	0.8-1.2	-	0.015-0.06	-	-	0.09-0.13
ZIRLO®	USA	0.9-1.13	0.9-1.2	0.1	-	-	0.09-0.15
MDA	Japan	0.5	0.8	0.2	0.1	-	-
HANA-3	Korea	1.5	0.4	0.1	-	0.1	
HANA-4	Korea	1.5	0.4	0.2	0.1	-	0.12
HANA-5	Korea	0.5	0.8	0.35	0.15	0.1	
HANA-6	Korea	1.1	-	-	-	0.05	

2.2.3. Plastic Anisotropy in hcp metals

Most of the metals especially those having cubic crystal structure have random orientations of grains giving them isotropic mechanical properties. However, this is not the case for hcp metals.

Due to a limited number of slip systems present, mechanical working or thermal treatment is sufficient to make these materials anisotropic.

The Hill's equation for anisotropic material is given as follows:

$$F(\sigma_y - \sigma_z)^2 + G(\sigma_z - \sigma_x)^2 + H(\sigma_x - \sigma_y)^2 + 2L\tau_{yz}^2 + 2M\tau_{zx}^2 + 2N\tau_{xy}^2 = 1$$

where F, G and H are functions of material yield strengths and σ_x , σ_y and σ_z are principal stresses along normal, transverse and rolling directions respectively . This is also the generalized form of Von-Mises criterion. Later, this equation was modified by Backofen by defining

R=$\frac{F}{H}$ and P=$\frac{F}{G}$

Following the convention adopted by Woods and Duncombe [19], a generalized stress is defined as the uniaxial yield stress along the rolling direction which is as follows:

$$\sigma_g = \frac{R(\sigma_r - \sigma_\theta)^2 + RP(\sigma_\theta - \sigma_z)^2 + P(\sigma_z - \sigma_r)^2}{P(R+1)}$$

For thin tube, radial stress can be assumed to be zero,

$$\sigma_g = \left(\frac{R\alpha^2 + (\alpha-1)^2 RP + P}{P(R+1)}\right)^{1/2} \sigma_z \qquad (2.10)$$

The degree of anisotropy can be quantitatively known by R and P parameters which are defined as:

$$R = \left(\frac{\dot{\varepsilon}_\theta}{\dot{\varepsilon}_r}\right)_{\varepsilon_z}, \sigma_\theta = \sigma_r = 0 \qquad (2.11)$$

$$P = \left(\frac{\dot{\varepsilon}_z}{\dot{\varepsilon}_r}\right)_{\varepsilon_\theta}, \sigma_z = \sigma_r = 0 \qquad (2.12)$$

Where, $\dot{\varepsilon}_\theta$ and $\dot{\varepsilon}_r$ are strain rates in hoop and radial directions respectively [20].

These parameters also define the wall thinning resistance of an isotropic material and thus control the formability. Formability of these textured materials is characterized by the Backofen formability parameter (B) [21] defined as:

$$B=\sqrt{\frac{(R+1)(R+4RP+P)}{4R(R+P+1)}} \tag{2.13}$$

2.2.4. Crystalline Orientation Distribution Function

Macroscopic texture can be used to qualitatively describe the anisotropic mechanical properties of hcp metals. ODF describes the volume fraction of crystallites having the orientation of the crystal axis with reference to a fixed coordinate system (RD, TD, and ND). ODF can be fitted by a series expansion with suitable mathematical functions. These functions are spherical harmonic functions [22].

$$\omega(\theta,\psi,\varphi)=\sum_{l=0}^{\infty}\sum_{m=-l}^{l}\sum_{n=-l}^{l}W_{lmn}Z_{lmn}(\cos\theta)e^{-im\emptyset}e^{-in\emptyset} \tag{2.14}$$

Where, W_{lmn} and Z_{lmn} are termed as series coefficients and augmented Jacobi polynomials, respectively.

The average property of a polycrystalline aggregate is given as

$$<\rho(\theta,\psi,\varphi)>=\int_0^{2\pi}\int_0^{2\pi}\int_{-1}^{1}\rho(\theta,\psi,\varphi)\ \omega(\theta,\psi,\varphi)d(\cos\theta)d\psi d\varphi \tag{2.15}$$

The experimental texture is measured in the form of pole figures. The information from the pole figure must be transformed to compute the ODF. The experimental texture can be measured with the help of X-ray diffraction (XRD) or Electron backscattered diffraction (EBSD). Under creep conditions such as here, strain rates are temperature- and stress-dependent; thus, uniform stress lower-bound analyses are applicable where stress equilibrium is maintained at the expense of strain (-rate) compatibility among crystallites [23].

The creep rate in power-law region is given by:

$$\dot{\gamma}^k = A\,(\frac{\tau}{\tau_0})^n \quad (2.16)$$

Here, A is the reference shear stress, τ_0 is the reference shear stress on *k*th slip system and n is the stress exponent. The total strain-rate in the crystal is the sum of the contribution from each active slip systems.

$$\dot{\varepsilon}^c{}_{ij} = \sum_K \mu_{ij}{}^k \dot{\gamma}^k \quad (2.17)$$

Where, μ_{ij} is the geometric tensor connecting slip co-ordinates with crystal co-ordinates.

Also,

$$\tau^k = \sigma_{ij}{}^c \mu_{ij}^k \quad (2.18)$$

2.3. Accident Tolerant Fuel Cladding

2.3.1. Fukushima Accident

In 2011, a tsunami wave spanning a height of 15 m hit three Fukushima Daiichi reactors [24]. After the fission reaction was stopped, the fission products were still in the radioactive state, hence they emitted beta, alpha and gamma rays. These rays produce what is called decay heat in the reactor. Hence, the coolant needed to be kept circulating to cool the reactor. The diesel generators, which were planned to be used as an emergency backup for circulating the coolant in the reactor failed. Because of failure of heat removal by circulation to an outside heat exchanger, the temperature close to the zirconium cladding rose to about 1200^0 C. Zirconium oxidizes easily above 1200^0 C, reacting with water to release hydrogen and forming ZrO_2. This reaction is exothermic and produces large amounts of heat and hydrogen [25].

$$Zr + 2H_2O \rightarrow ZrO_2 + 2H_2 \quad (2.19)$$

This is called a loss of coolant accident (LOCA). The amount of generated hydrogen gas blew off the containment rooftop. Due to severe oxidation, the Zr cladding failed and lead to the release of radioactivity to the environment.

Table 2.3. The contribution of the decay heat (in bold) to the total heat produced in the reactor [26].

	Energy from Fission (MeV)	Recoverable in Core (MeV)
Prompt:		
kinetic energy of fission fragments	168	168
kinetic energy of prompt fission neutrons	5	5
Fission γ rays	7	7
γ rays from neutron capture	...	3-9
Delayed:		
fission product β–decay energy	**8**	**8**
fission product γ–decay energy	**7**	**7**
neutrino kinetic energy	12	0
Total energy (MeV)	207	198-204

2.3.2. Desirable Properties of fuel and Cladding Materials

The cladding material and fuel are the main components of the reactor. Ideally, these components should be able to adapt to any changes that take place in a reactor i.e LOCA or station blackout. Unfortunately, a property which is desirable under normal condition may not be desirable under other conditions. Table 2.4 shows the desirable properties under a different set of operating temperatures.

Table 2.4. Desirable properties of fuel and cladding materials under different conditions, NR: Normal Reactor, PO: operational Power ramps, H stands for High and L for Low [27].

Cladding				**Fuel Pellet**		
Properties	**NR**	**PO**	**LOCA**	**NR**	**PO**	**LOCA**
Thermal Conductivity	H	H	H	H	H	H
Heat Capacity	-	-	H	-	-	H
Oxidation rate	L	L	L	-	-	L
Coefficient of thermal expansion	-	-	-	-	L	-
Creep rate	H	H	L	H	H	-
Strength	H	H	H	-	L	-

As depicted in table 2.4, adequate but not excessive, creep in both components and high cladding strength are desired under normal operating conditions to avoid and withstand stress buildup in the cladding. Minimization of cladding corrosion to avoid thickness loss in the load-bearing cladding tube is desirable. Under power ramps, high thermal conductivity and creep rates along with a low coefficient of thermal expansion are desirable in the fuel pellet to minimize pellet cladding mechanical interaction (PCMI). In the cladding, high strength along with the ability to accommodate pellet expansion via creep is highly desirable. For a design basis LOCA, high thermal conductivity is desirable in the fuel and the cladding to reduce the thermal energy stored in the pin. At the same time, high heat capacity is also desirable since it will reduce the rate of temperature rise as a result of decay heat. During LOCA, of great importance is the reduction of cladding oxidation rate to limit its degradation during accident progression and loss of post-quench ductility. Cladding creep resistance is highly desirable to delay fuel rod burst and ballooning [27].

2.3.3. Candidates for accident tolerant cladding materials

Despite extensive research, we are still far away from the ideal cladding material for nuclear reactors. At one time, Zircaloy was thought to be the ideal material but after the LOCA accident in Fukushima that's not the case due to its poor oxidation resistance above 1200 ^{0}C. FeCrAl appears to be the closest candidate to replace Zircaloy in terms of the work carried out, ease of availability and low cost however the data on its high-temperature properties is limited which needs attention. More research is needed on chromium-coated zirconium to comment on its feasibility.

Table 2.5. Summary of relevant data for cladding material options [28].

Clad Material	**Density [g/cm^3]**	**Composition [wt.%]**	**$\sum^{thermal\ abs}$ [cm^{-1}]**	**POR constant in 1200 ^{0}C steam [mg]**
Zircaloy	6.56	98.26 Zr, 1.49 Sn, 0.15 Fe, 0.1 Cr	0.0028	$6.5x10^{-4}$
304SS	7.9	71.35 Fe, 18.9 Cr, 8.35 Ni, 0.7 Mn, 0.42 Si, 0.27 Mo	0.078	$8.5x10^{-4}$
310SS	8.03	52.55 Fe, 25.22 Cr, 19.51 Ni, 1.9 Mn, 0.7 Si, 0.12 Mo	0.0880	$1.3x10^{-5}$
FeCrAl	7.1	75 Fe, 20 Cr, 5 Al	0.0634	$1.8x10^{-6}$
SiC	2.58	70.08 Si, 29.92 C	0.0021	$3.7x10^{-7}$

From table 2.5, It is clear that SiC has the lowest thermal absorption cross-section followed by Zircaloy. Steels have high thermal neutron absorption cross-sections. SiC/SiC composites are anticipated to provide additional benefits over zirconium alloys: they provide smaller neutron absorption cross sections, general chemical inertness, ability to withstand higher fuel burn-ups and higher temperatures, exceptional inherent radiation resistance, lack of progressive irradiation growth and low induced activation/low decay heat. Moreover, SiC is considered to be permanently stable in nuclear waste [29].

Although SiC-based cladding appears to be attractive, critical feasibility issues such as hydrothermal corrosion, potential loss of fission gas retention due to cracking under normal operation conditions, development of fuel performance modeling capability and high processing cost must be addressed. Low thermal conductivity in SiC leads to elevated fuel temperatures and large temperature gradients across the cladding that in turn induces large thermal stresses across

the cladding thickness [30]. Although SiC/SiC composites are deemed the ideal ATC material, a lot of research is needed to overcome their current limitations.

2.3.4. Fe-based cladding materials

Previously, various 300-series Fe-Cr-Ni based stainless steel variants (304, 316, 347, 348, etc.) have been used as nuclear fuel cladding in several LWRs because of their low cost compared to Zirconium alloys. The alloying element Ni has high thermal absorption cross-section and hence, reactors gradually migrated away from using steel cladding [31].

The operation of stainless-steel cladding is generally thought to have been successful, at least for PWRs, despite several fuel failures. Many of the problems with this cladding were eventually addressed, but not before a significant transition to zircaloy cladding had already started [32].

Fuel failures from the La Crosse BWR were generally attributed to PCMI and intergranular stress corrosion cracking, similar to failures from Big Rock Point, Dresden-1, and Humbolt Bay. After the implementation of power restrictions, the cladding failure rate decreased. These examples of stainless steel cladding failure, in particular at the Connecticut Yankee PWR and the La Crosse BWR, demonstrate that the stainless-steel cladding was not necessarily the limiting factor. It should also be pointed out that these fuel rods were operated at comparatively lower linear heat rates (maximum average LHR at 15 kW/m) than zircaloy-cladded fuel (~%75), however many did not contain the fuel rod pre-pressurization, fuel pellet dishing and chamfering, and ramp rate restrictions that are exercised today [33].

Based on the above arguments, it is just a mere coincidence that the time when stainless steel fuel cladding was retired, there was a remarkable reduction to the fuel failure rate. It had

nothing to do with the replacement of stainless-steel cladding but mostly everything to do with improved operational guidelines.

2.3.5. FeCrAl

First Fe-Cr-Al alloy, KANTHAL® was invented by Hans von Kantzow in Sweden in the 1930's [34]. These alloys generally have up to 22% Cr. But high Cr has been found to nucleate alpha prime phase known to cause 475^{o}C embrittlement. Total Elimination of Cr is not possible because the minimum 12% Cr is necessary for sufficient oxidation resistance. G.Bonny et al [35] using Calphad calculations recently predicted that Al additions are beneficial to get rid of 475^{0} C embrittlement. Hence, for fuel cladding applications lean Cr (12-14%) and 4-6% Al compositions have been chosen. Also, some yittria is added to maintain high-temperature oxidation resistance to compensate for low Cr in these alloys. These alloys are different than the austenitic stainless steels described in the last section. Recent tests have shown that high chromium ferritic, BCC alloys offer superior stress corrosion cracking resistance compared to austenitic steels like the 300-series stainless steel variants described in section 2.3.4 [32]. Also, Ferritic steels have some advantages in void swelling, thermal properties and strength at elevated temperature, compared to austenitic steels [36]. Additionally, it is well known that Oxide Dispersion Strengthened alloys have a major advantage in terms of void swelling under irradiation. Hence, ODS FeCrAl is also being considered for Accident Tolerant fuel cladding application.

As previously discussed, the increased parasitic neutron absorption of FeCrAl compared to Zircaloy is a major challenge if Zircaloy has to be replaced by FeCrAl. The current cladding thickness of zirconium alloys is close to 600μm For FeCrAl to have similar neutron absorption the calculated cladding thickness is around 300μm [37]. Since FeCrAl has high strength compared to Zr this thin cladding requirement is possible and has been achieved. There are still some issues

which need attention before FeCrAl goes on to be used as a cladding material in commercial reactors. Firstly, FeCrAl cladding may release more tritium to the coolant than Zirconium alloys one solution for this problem might be coating inside part of the tube with alumina [38]. Second is the alpha prime precipitation in FeCrAl after neutron irradiation which is still under investigation, a recent study by Zinkle et al [39] found that ODS FeCrAl has an order of magnitude less alpha prime precipitation than conventional FeCrAl alloys which is promising.

2.3.6. Oxidation Behavior of FeCrAl

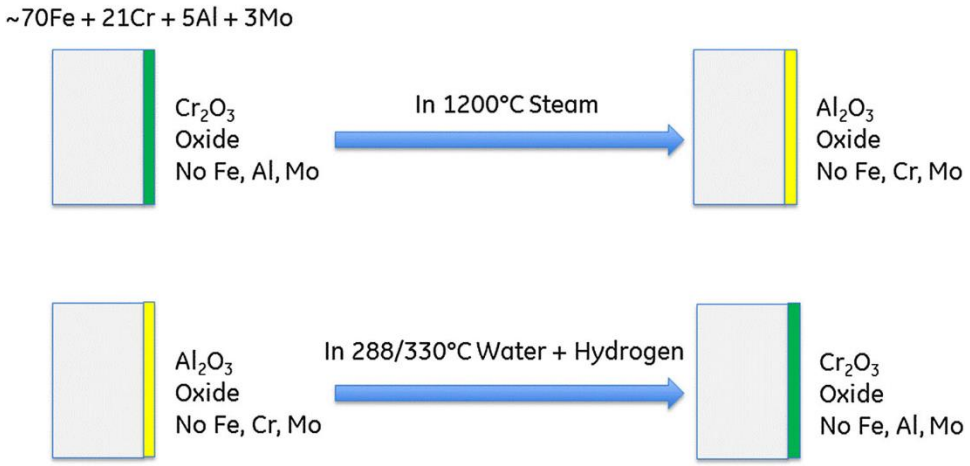

Figure 2.6. Versatile oxide layers present in FeCrAl to help cope with LOCA [40].

FeCrAl alloys are thought to possess excellent oxidation resistance up to 1500^{o}C (close to its M.P). If the FeCrAl tube has an alumina layer on the surface, it will dissolve in high-temperature (300^{o}C) water and a protective Cr oxide will form in its place. If FeCrAl tube has a Cr oxide on the surface and it is exposed to accident steam conditions, the Cr oxide layer will evaporate, and an alumina layer will form to protect the tube. So, Cr protects the alloy under normal Operation conditions and Al protects the alloy at temperatures higher than 1100 ^{o}C.

J. Engkvist et al [41] studied the influence of Al-concentration on oxide layer characteristics of FeCrAl. In this study, alloys containing 20 wt% Cr and varying aluminum content from 1.2-5 wt% were oxidized at 900^0 C for 72 hrs. They found out that a critical aluminum concentration of 3.2% was necessary to form a continuous and Protective Alumina layer.

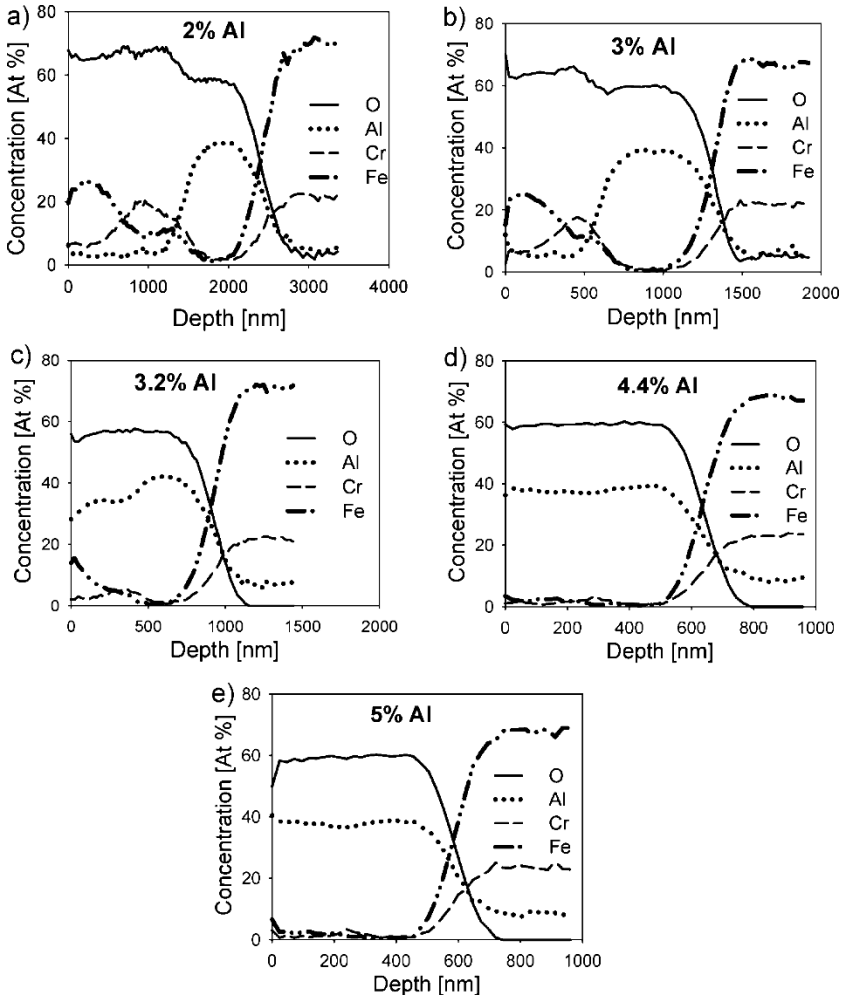

Figure 2.7. Auger electron spectroscopy (AES) of various elements present in the oxide layers [41].

The figure clearly shows that For the 1.2 wt% Al alloy a complex oxide is formed with an outer Cr- and Mn based oxide layer, For the 2.0 wt% and 3.0 wt% alloys a three-layered oxide

scale formed most stable alumina at the inner interface, the secondly most stable chromia in the center and the less stable iron-based oxide at the outer surface. For alloys greater than 3.2 wt% Al, a smooth and continuous alumina film forms on the surface followed by a mixed layer of Chromia and iron oxide. The surface morphology of the formed oxide layers becomes smoother and the oxide grain structure becomes finer with increasing Al-concentration in the FeCrAl alloy.

2.3.7. Manufacturing of FeCrAl tubes

Model FeCrAl alloys for cladding application

The newly developed nuclear grade FeCrAl alloys by Oak Ridge National Laboratory (ORNL) are called as model FeCrAl alloys. Tube drawing of model FeCrAl alloys is planned by using tube drawing or Pilgering operation. Tube drawing is known to induce tensile stresses in the material whereas Pilgering is known to induce compressive stresses in the material the latter being beneficial for cladding material. Extensive work has been carried out by Yamamoto et al for design and property based evaluation of many model FeCrAl alloys and shortlisting a few for cladding application [42].

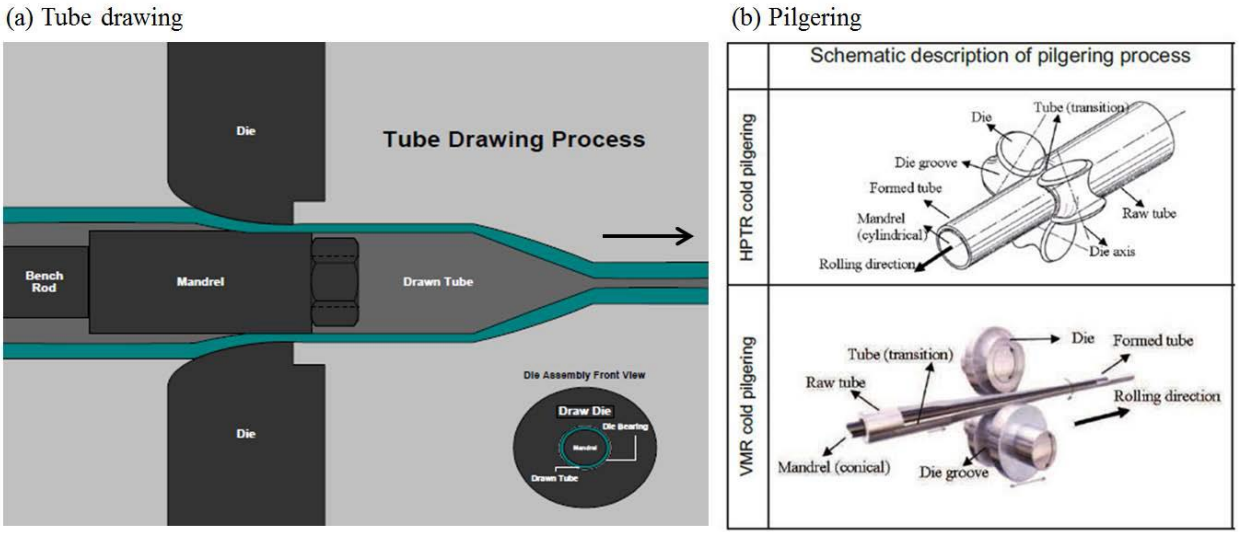

Figure 2.8 .Two major tube drawing process a. Tube drawing [58], b. Pilgering [59].

The work for alloy development was divided into 2 phases. In Phase 1, utilizing the thermodynamic data various alloy compositions were selected, and the alloys were cast by arc-melting in a back-filled argon gas atmosphere with pure element feedstock and/or pre-alloyed Y-Al to make 400-800 g button ingots. Various alloy series standard were developed by ORNL for model FeCrAl alloys. In case of "B series" alloys, the first two numbers in the alloy designation refer to nominal target Cr composition while the third number refers to nominal Al Composition. In phase 2 minor alloying elements such as Mo, Si, Nb and/or C were added to introduce solid-solution strengthening and precipitation hardening. For more detail's reader may refer to [42].

2.3.8. Burst behavior of Zr and FeCrAl under LOCA

A study was performed by Terrani et al [43] which aimed at stimulating burst behavior of Zircaloy and FeCrAl under LOCA. The tubings of both these materials were filled with zirconia pellets and were internally pressurized at room temperature then subjected to temperature ramping of 5^0 C/s from 300 to 1200 C, holding at 1200°C for 3 min, ramp-down to 800°C (~5°C/s), and finally, quenching with room temperature water. It was observed that both the materials had different failure modes. Zr tube ballooned and failed at the point of minimum thickness whereas unlike Zr-based alloys, cladding cross-sectional area of FeCrAl remained largely unchanged up to the point of burst. Therefore, for a given rod internal pressure, the temperature onset of burst in Fe-based alloys appears to be simply a function of the alloy's ultimate tensile strength, particularly at high rod internal pressures.

Maintaining a coolable core geometry is an important requirement for any cladding, one aspect of which involves the possibility of flow blockage due to excessive ballooning of the cladding. Although for the Fe-based alloys large burst openings are observed, this does not necessarily result in flow blockage. In fact, the most severe cases of blockage result from excessive

ballooning with a small burst opening. As shown in Figs. 2.9, the large burst openings in Fe-based alloys may accommodate coolant flow past the rod [43].

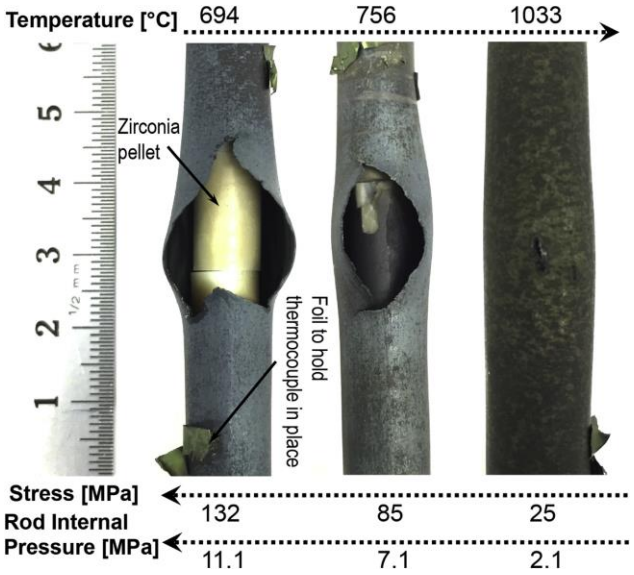

Figure 2.9. Post burst photographs of Fe-13Cr-5Al for three different burst conditions [42].

2.4. Creep Studies on FeCrAl

Research on FeCrAl alloys for cladding is ~50 years old and ODS FeCrAl was first commercialized more than 30 years ago [44,45]. Not a lot of creep studies have been done at low stresses and LWR temperatures. Since the creep rate at that stresses and temperatures are thought to be pretty low. A study carried out in the 1980s by Jones et al [46] found n value of 5.5-5.8 in the temperature range of 650-800 ^{0}C suggesting dislocation climb mechanism. They saw a transition in activation energy at the Curie temperature which they claim as 710^0 C for their alloy and explained it on the basis of change in lattice diffusivity at Curie temperature. Table 2.6 shows the Curie temperature of various new FeCrAl grades.

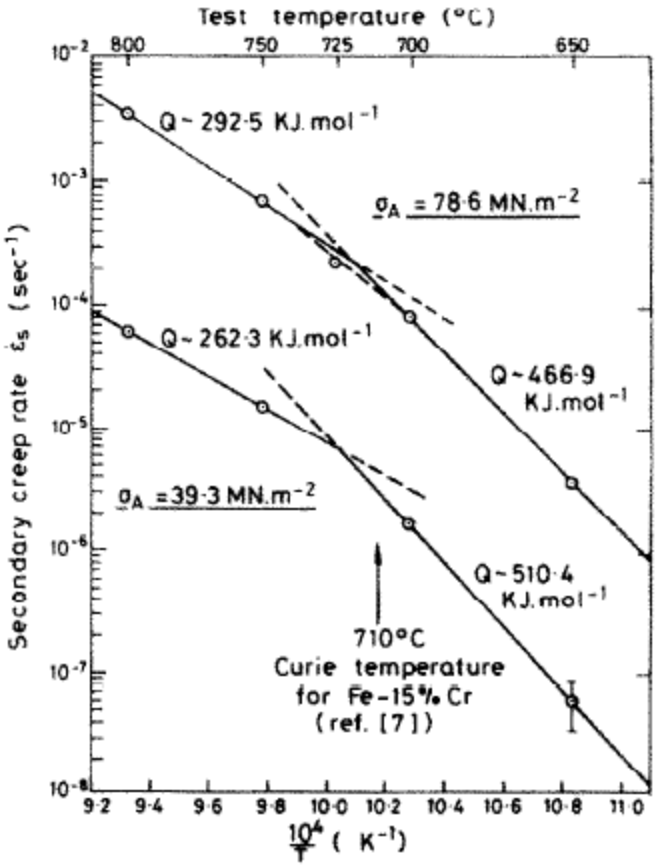

Figure 2.10. Transition in activation energy at Curie temperature for fecralloy stainless steel [46].

Table 2.6. Curie Temperature of various FeCrAl grades [47].

Alloy ID	**Cr, Al (wt%)**	**T_C (K)**
Kanthal APMT	21,5	852
C06M	10,6	888
C35M	13,5	870
C36M	13,6	771

Whittenberg [45] tried some creep tests on ODS MA 956-E (20 Cr, 4.5 Al) alloy at 1092^0 C. He reported that MA-956E does not easily undergo slow plastic deformation. Rather than deform under creep loading conditions, the alloy apparently fails by a crack nucleation and growth

mechanism and there appears to be threshold stress below which crack nucleation and/or growth does not occur.

Table 2.7. Compilation of creep activation energy for FeCrAl (UNS: unspecified).

Material	**Cr,Al (wt%)**	**Temp Range (^{0}C)**	**n**	**Q (kJ/mol)**	**Stress regime (MPa)**	**Ref**
T35 AY	13,5	UNS	3.7-3.9	248-258	UNS	[48]
C35M, C35MN	13,5	<600 800	5.5 10	247 -	UNS 20-26	[43,49]
Fecralloy 1	22,5	500-1100	5.5	392	UNS	[50]
Fecralloy 2	14,4.5	>725	5.5	277	<100	[46]
Fecralloy 2	14,4.5	<710	5.8	489	<100	[46]
Fecralloy 2	14,4.5	<710	10.5	489	>100	[46]
Fecralloy 3	UNS	UNS	5.29	486	UNS	[51]
KANTHAL-AF	21,5	UNS	4.5	143	UNS	[48]

CHAPTER 3- EXPERIMENTAL PROCEDURE

3.1. Biaxial creep test of HANA-4

3.1.1. Materials and methods

HANA-4 alloy tube used in the present investigation was received from KAERI in CWSR condition. The average outer diameter and thickness of the tubes were 9.43mm and 0.6 mm respectively which were measured by Vernier Caliper.

Table 3.1. Composition of HANA-4.

Materials	**Country of Origin**	**Nb**	**Sn**	**Fe**	**Cr**	**Cu**	**O**
HANA-4	Korea	1.5	0.4	0.2	0.1	-	0.12

3.1.2. Creep Test Specimen

Each sample for creep tests had a length of around 117 mm. Fig 2. Shows the sample and the brass mandrel that was inserted into the tubing during biaxial creep test. There is a possibility of tube burst on the application of high gas pressure, but when the mandrel is inserted into the tube the low gas volume (due to mandrel) present in the tube will not cause serious accidents.

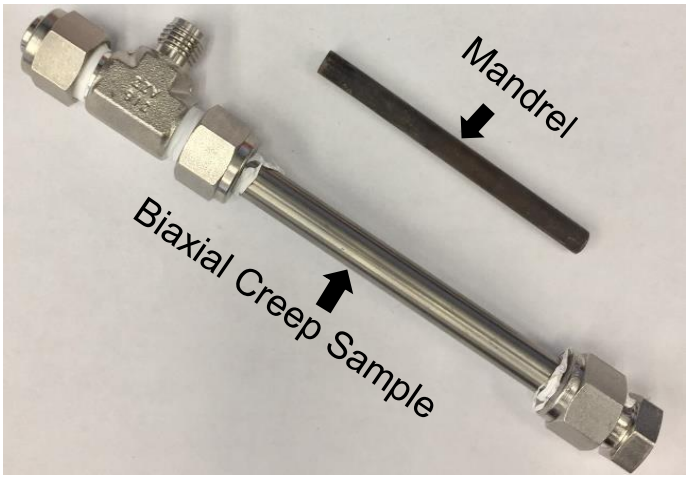

Figure 3.1. Biaxial creep sample along with brass mandrel.

3.1.3. Creep Testing Equipment

The biaxial creep experiments were conducted on an ATS® model-2330 lever arm (ratio 20:1) machine in combination with an internal pressurization system, which floods the hollow tube with argon gas (Figure 3.2). Biaxial creep Tests were performed for the stress ratios of 0, 0.5,1 and 2 at each stress ratio, 5-6 different stresses were applied. These tests at different stresses were performed until a steady state was achieved. The temperature was monitored with the help of a K-type thermocouple placed at the center of the sample. The gauge length of the sample was 1 inch. The axial and hoop displacement data were continuously logged into a computer using a data acquisition system. . Note that the axial steady-state creep rate was not recorded for a stress ratio of 2, this is because it was assumed that the axial creep rate is negligible compared to the hoop creep rate. Also, for the uniaxial experiments, the hoop creep rate was not obtained. The hoop strain is expected to be negligible in axial loading conditions.

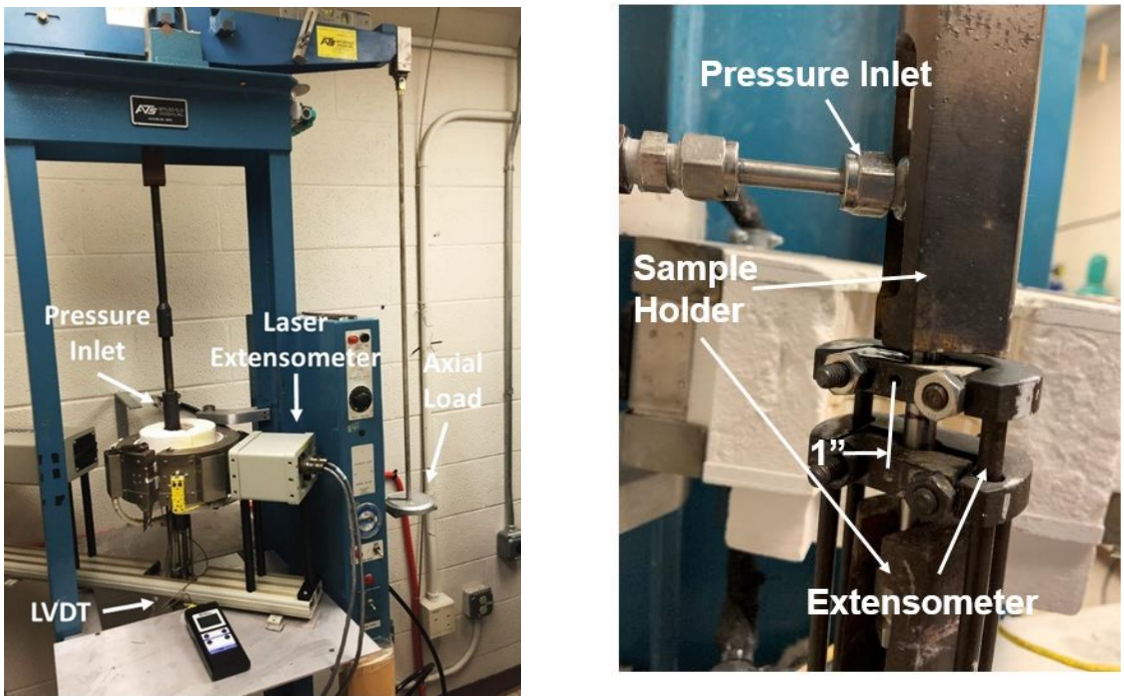

Figure 3.2. Biaxial creep test setup.

3.1.4. Creep Test data Acquisition

During each creep test, the circumferential and the axial strains were measured at a point where the specimen temperature was known and maintained. To measure the hoop strain, a laser measurement device was used (see Figure 3.2). The Techmet® LaserMike™ Model 162 consists of two parts, a laser emitter, and a receiver. As shown in Figure 3.3, the uninterrupted width of the laser beam is known by the receiver and when the specimen is placed into its path, a portion of the center of the laser beam is blocked. This portion corresponds to the diameter (d) of the specimen. The voltage signal is generated based on the portion of the laser that is blocked. Care was taken to keep the sample straight and not bent at an angle as this might introduce error in the reading.

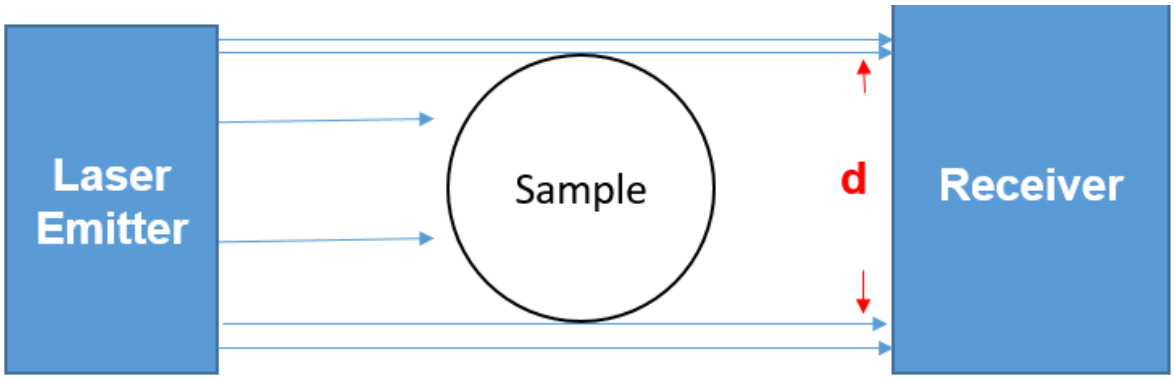

Figure 3.3. Schematic of diameter measurement by non-contact laser extensometer.

Linear Variable Displacement Transformer (LVDT) was used to measure the axial strain with a resolution of about 20µm as seen in Figure 3.2.

3.1.5 Electro-polishing

For characterizing samples using EBSD (Electron Backscattered Diffraction) and FIB-SEM (Focused Ion Beam-Scanning Electron Microscope), HANA-4 samples were first polished on a polishing machine to mirror finish and then subjected to electro polishing. The width of the polished sample had to be pretty small for the sample to fit in the electropolishing sample holder. The equipment is shown in figure 3.4.

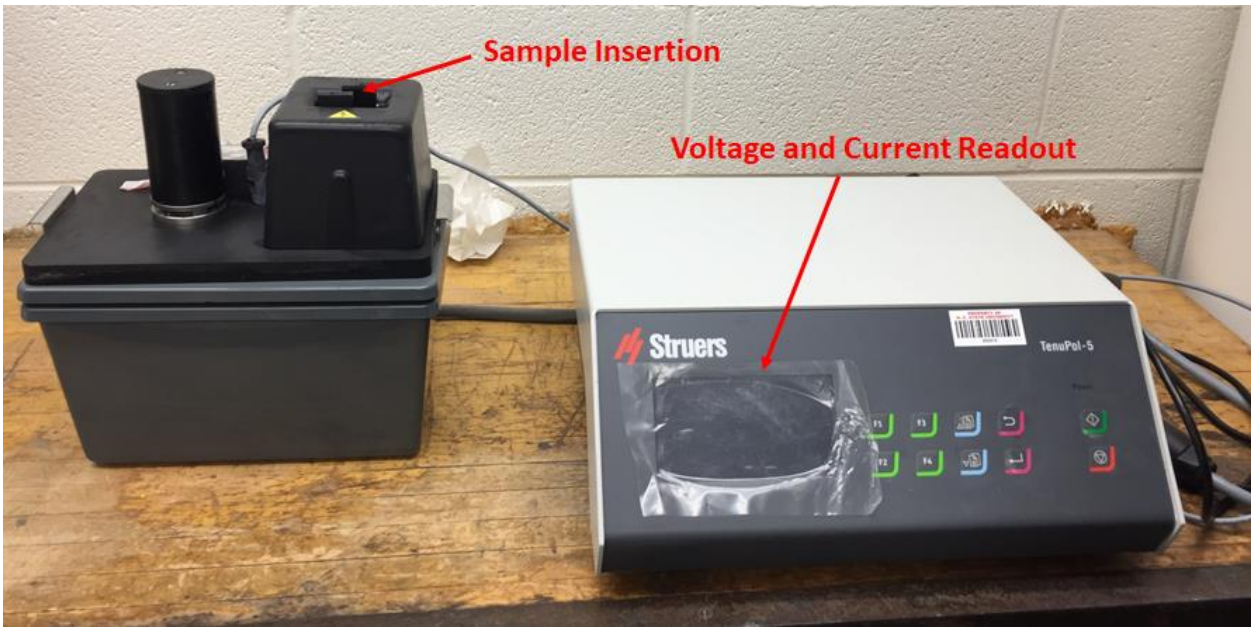

Figure 3.4. Electro-polishing equipment used to prepare a sample for characterization.

The samples were prepared using the twin-jet electropolishing technique at −35 °C and 17.5 V for a duration of about 1 min in an electrolytic solution consisting of 5% per chloric acid and 95% methanol. The samples used for optical microscopy and SEM are shown below.

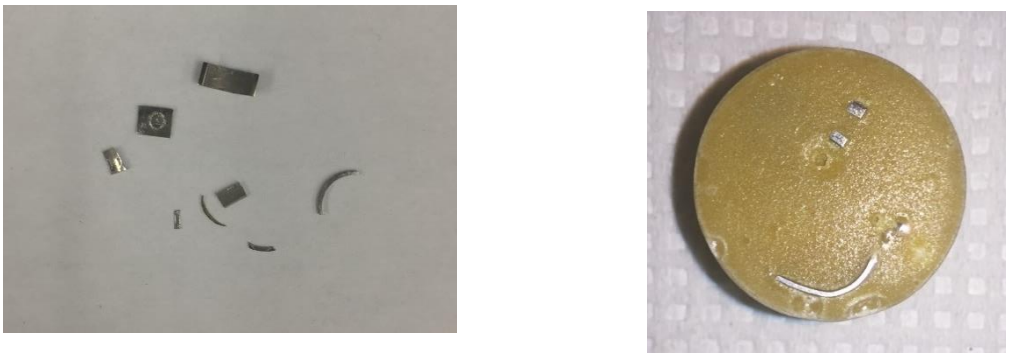

Figure 3.5. Samples used for FIB-SEM, EBSD (left) and optical microscopy (right).

3.1.6. Equipment for EBSD/FIB

EBSD was performed on Field Emission Scanning Electron Microscope – FEI Verios 460L equipped with a detector named "**Symmetry**", providing superior orientation microscopy capabilities. Speeds up to 3200 pixels/second are achievable, even at reduced operating voltages and beam currents. This equipment is a part of the Analytical Instrumentation Facility (AIF) at NC State University.

Figure 3.6. VERIOS SEM equipped with EBSD at AIF.

Focused-Ion-Beam was used to get the general tube microstructure along axial, hoop and radial directions. This technique is especially useful for textured material as the ion beam etches away etch grain according to the grain orientation and due to contrast generated the grains become visible. This equipment is also part of AIF.

3.2. FeCrAl

3.2.1. Burst test specimen

Burst testing was performed using a sustained gas pressurization system (ATS model 1815) capable of gas pressurization to about 17,000 psi the same one that was used for biaxial creep test. Figure 3.7 shows a typical C26M2 burst specimen before the test. Burst test specimens were 12.7 mm (5") in length. The average outer diameter of the tubes was 9.46 mm and the thickness was 0.39 mm. On both ends, 3/8" Swagelok fittings were installed and a mandrel was inserted into the center to decrease the volume of high-pressure gas within.

Table 3.2 Chemical composition of FeCrAl-C26M2 tubes

Element	**Cr**	**Al**	**Mo**	**Si**	**Y**	**Fe**
Wt %	12	6	2	0.2	0.05	Bal

Figure 3.7. FeCrAl sample used for burst testing.

Etchant for FeCrAl Microstructure

The etchant used was freshly prepared glyceragia: Hydrochloric acid 15ml; Nitric acid - 5ml; Glycerol - 10ml.

The sample was swabbed with cotton for 0.5-1 min. Glyceragia was not stored.

3.2.2. Data acquisition

A web-camera was attached in front of the pressure gauge. This camera was connected to a laptop equipped with Webcam looker (a motion detection software) which was used to accurately detect the rupture time (t_r) and was used to monitor pressure leaks before starting the test. Figure 3.8 shows this equipment. Two thermocouples were utilized to check the sample temperature one connected at the top and another at the bottom of the sample. The furnace used was capable of reaching temperatures up to 1273 K.

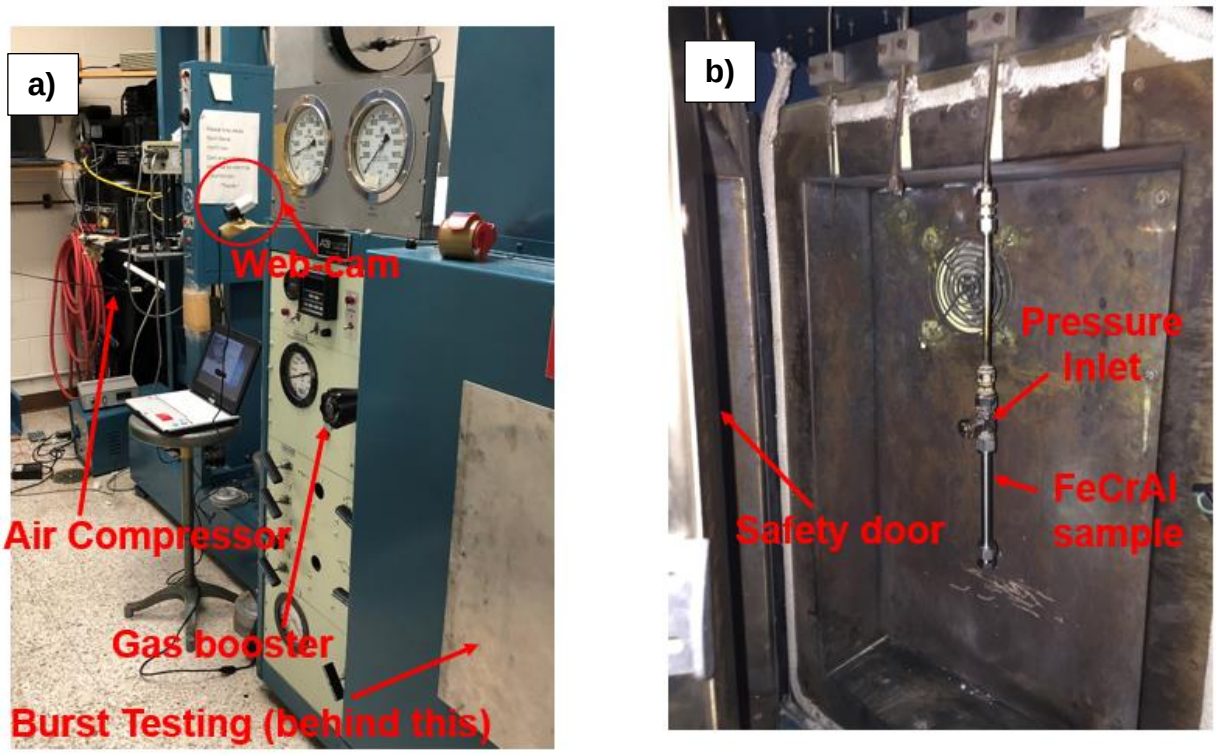

Figure 3.8. Burst testing equipment a) From front, b) From back, c) Image captured by webcam during a sample rupture and d) Furnace used for burst test.

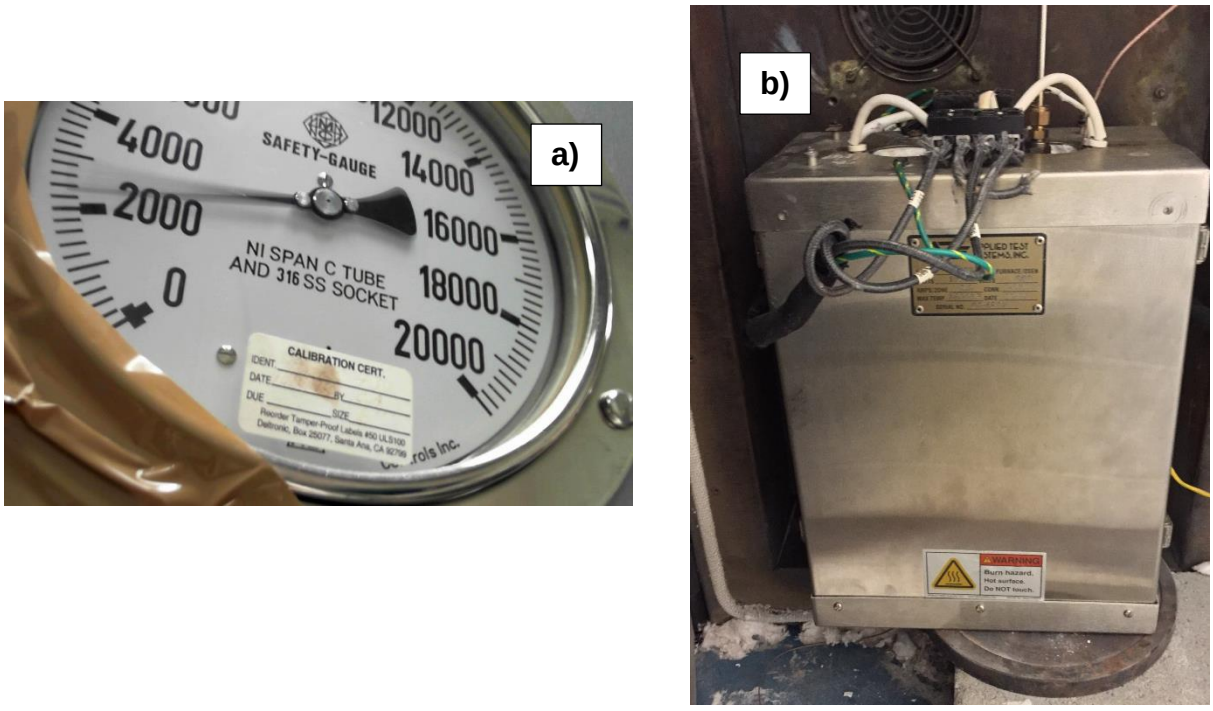

Figure 3.9. a) Image captured by webcam during a sample rupture and b) Furnace used for burst test.

CHAPTER 4 -CALCULATIONS

4.1. Stresses in a thin-walled tube

A thin-wall approximation was applied to the HANA-4 tubing in the calculation of axial and hoop stresses because the wall thickness (t) to outer diameter (Do) ratio was less than 0.1. The radial stress can be assumed to be negligible due to the geometry of the tube. Biaxial stress state was imposed by applying axial load and closed-end internal pressurization of the HANA-4 tubes using argon gas. Biaxial creep tests were carried out at different stress ratios (α) defined as

$$\alpha = \frac{\sigma_\theta}{\sigma_z} \tag{4.1}$$

Where σ_θ and σ_z are hoop and axial stresses respectively.

The hoop stress is given by:

$$\sigma_\theta = \frac{P({D_0}^2 + {D_i}^2)}{D_0^2 - D_i^2} \tag{4.2}$$

Where P is applied pressure, D_0 and D_i are outer and inner tube diameters.

The axial stress is given by:

$$\sigma_z = \frac{\sigma_\theta}{2} + \frac{4W}{\pi(D_o^2 - D_i^2)} \tag{4.3}$$

where W is applied axial load to the sample [22].

A value of α=0 corresponds to a pure axial load where α=2 indicated stress only from internal pressurization.

4.2. Creep strain calculation

Before starting the test, the LVDT used was calibrated. LVDT was fixed on the extensometer. The movable part (spring) of LVDT was displaced by a fixed distance and the corresponding change in voltage was recorded. For accuracy, the calibration was performed at small distances and many data points for a voltage corresponding to a fix displacement were generated. This data was plotted

in Excel™ and the equation between displacement and voltage was recorded. This was used to get the engineering axial strain (e_z). It was converted to true axial strain (ε_z) by using equation 4.4.

$$\varepsilon_Z = \ln(1 + e_Z) \quad (4.4)$$

This true strain was then plotted with respect to time. The slope of this curve in the steady-state region gave the value of steady state strain rate. The steady state attained was verified by taking derivative of strain vs time curve and seeing if it had attained a minimum value.

For measuring true hoop strain, a similar procedure was used. To analyze data in these plots ORIGIN software was used.

4.3. Grain shape calculations

To measure the grain-shape anisotropy from optical microstructure Image-J software was used. The image was first converted to 8-bit. Later, Image threshold was adjusted such that only grain boundaries were particularly visible. Then through the measure option in Image J. major and minor axis of grains were measured, the ratio of which gave measure of elongation for each grain.

4.4. Generating creep loci from texture coefficients

The CODF code was saved in a folder. The texture file from EBSD was opened with channel 5 to get the W_{lmn} values from l=0-16. These values were saved in a file named fdibodf.dat. Using the command prompt the directory of CODF was accessed by using command *cd name of the directory containing code*. The files RPB, BASAL, PRISM, RALPHA, PYRAMID were deleted before starting the program. The program was started typing *loci.exe*. The value of c/a ratio entered was 1.589. The value of n entered was 5 and a minimum number of pole figures required were inputted as 3. Afterward command *formal.exe* was executed and the same inputs as mentioned above were used. The results were saved in files RPB, BASAL, PRISM, RALPHA,

and PYRAMID. The first file gave R & P values for various slip systems and other 4 files gave the creep loci data assuming that Basal, prism or pyramidal slip system is active.

4.5. Burst Test Strain Calculations & Procedure

During the burst tests, the strain is not measured in situ as done during the creep tests. The total accumulated hoop strain is calculated from diametric measurements performed after rupture. Once the specimen has burst, the time to rupture is recorded and the specimen is removed from the furnace. After sufficient cooling, measurements along the diameter are taken away from the area of the fracture. A region of almost constant diameter was selected along the tube on both sides of the fracture and was averaged to produce the average diameter. The average diameter (d) and original diameter before test d_0 after testing was used in Equation 4.5 to arrive at the uniform circumferential elongation (UCE).

$$\text{UCE} = \ln\left(\frac{d}{d_o}\right) \tag{4.5}$$

The UCE was divided by Rupture Time (t_r) to get an approximate creep rate.

$$\dot{\varepsilon} = \frac{UCE}{t_r} \tag{4.6}$$

CHAPTER 5- RESULTS & DISCUSSIONS

5.1. Creep Curves

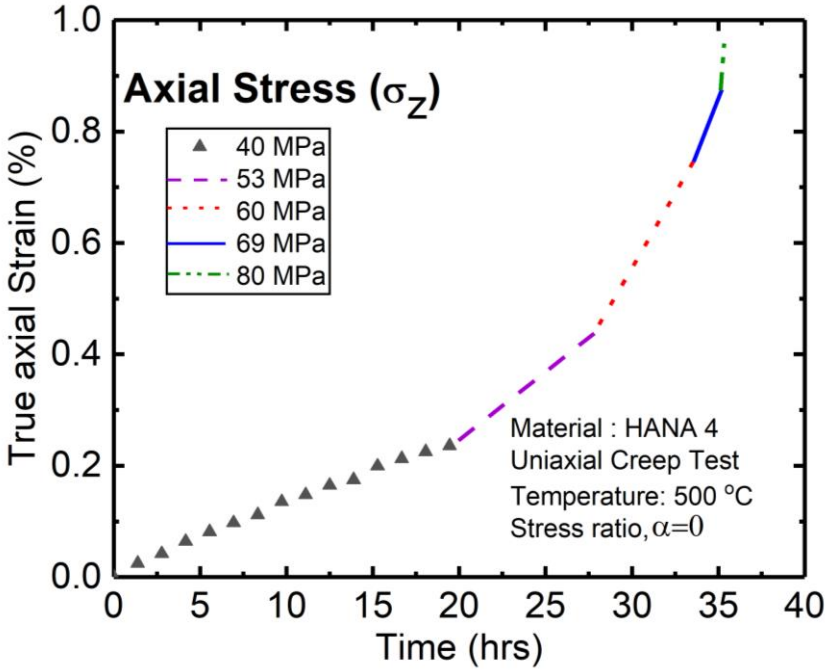

Figure 5.1. Creep curves from uniaxial creep test of HANA 4 at 500 ^{0}C.

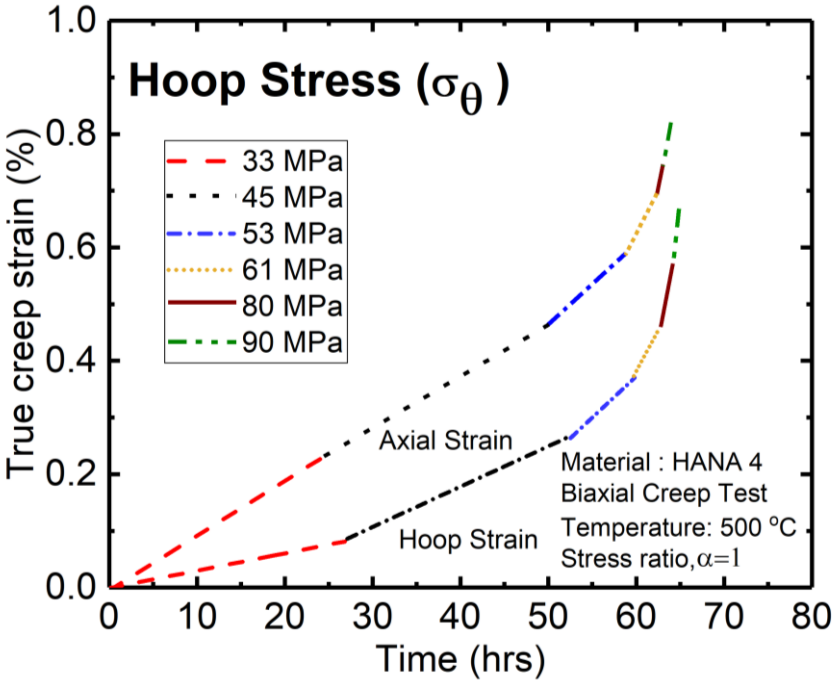

Figure 5.2. Creep curves from biaxial creep test of HANA 4 at 500 ^{0}C at stress ratio of 1.

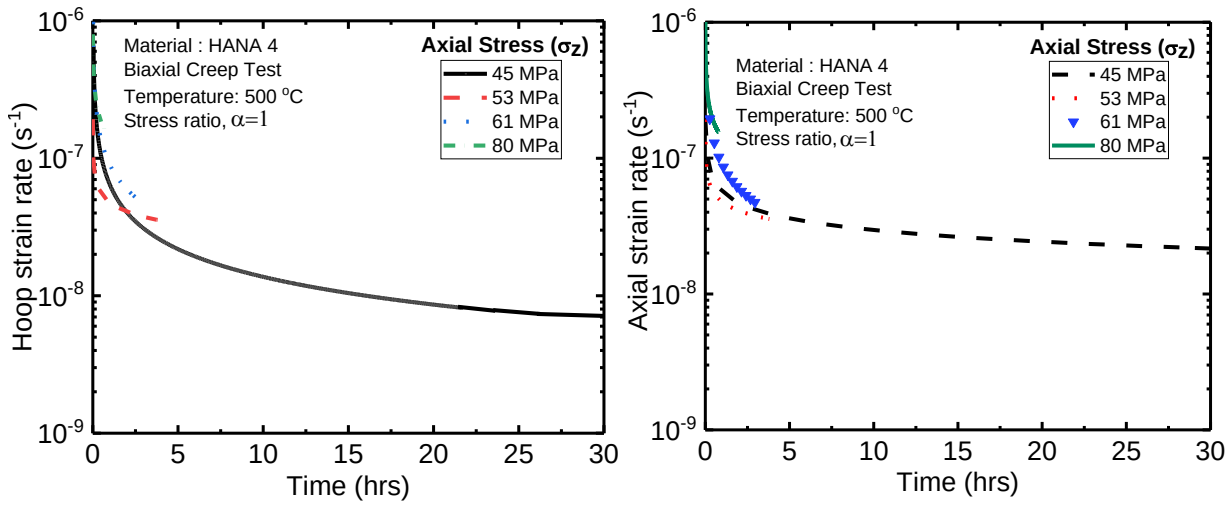

Figure 5.3. Strain rate vs time at various stresses at 500 ^{0}C for stress ratio of 1.

Figure 5.1 demonstrates uniaxial creep deformation characteristics of as-received HANA-4. As expected the steady-state creep rate increases as stress is increased. The steady-state creep rate for the stress of 40 MPa was noted to be about 3.28 x 10^{-8} s^{-1}, whereas it increased to 8.54 x 10^{-7} s^{-1} for the stress of 80 MPa

Figure 5.2 shows creep curves for stress ratio of 1 i.e. equibiaxial condition. The first derivative of creep strain w.r.t time is plotted in Figure 5.3 It was found that after some time the strain rate was almost constant which was used as an indicator to know when the steady state was reached. As expected, lower the stress more time is required to attain a steady state.

Figure 5.4 compares hoop and axial strains for various stresses. It must be noted that even though it looks like the axial strain is greater than hoop strain for almost all the stresses except 90 MPa. The difference between axial and hoop steady state strain rate is not that large. The ratio of the hoop to axial steady state strain rate ranges from 0.38 at 33 MPa to 1.49 at 90 MPa. So, for all practical purposes, in stress range of 53-90 MPa the rate of deformation along both directions can be assumed identical. At low axial stresses the deviation from this value can be attributed to

different creep mechanism(s) as seen from Figure 5.11, there are transitions in creep mechanisms from low to high axial stresses. Boopathy et al [1] have found the transitions in Rx-HANA4. They observed that at low stresses diffusion creep dominated at moderate stress levels rate controlling mechanism shifted to dislocation glide and at high stresses again changed to dislocation climb.

Figure 5.5 depicts the creep curves for stress ratio 2 i.e. only internal pressurization and no axial load. The axial strain measured was negligible and hence only hoop strain is shown.

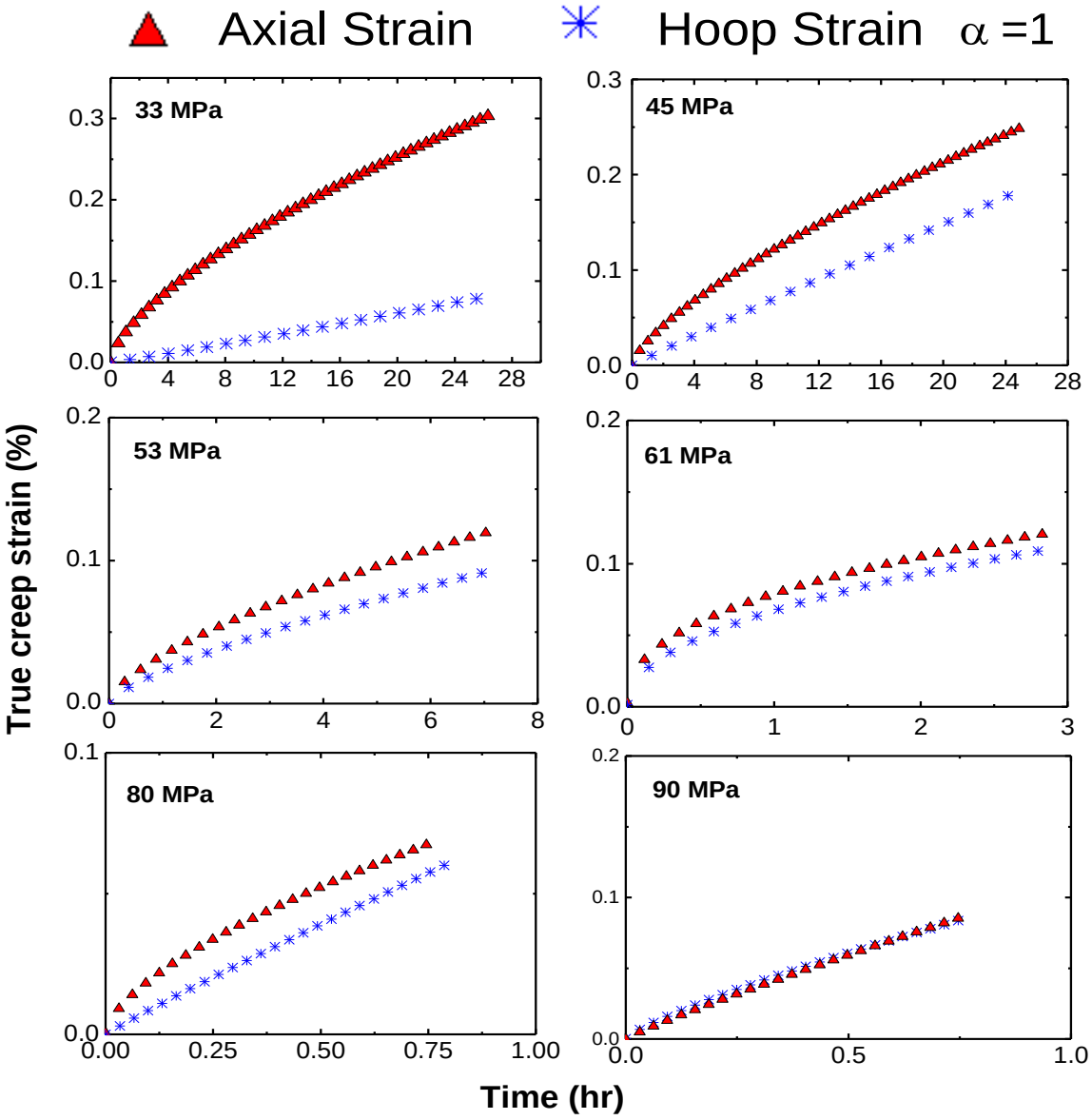

Figure 5.4. Comparison of hoop and axial strains at various stresses for stress ratio of 1 at 500 ^{0}C.

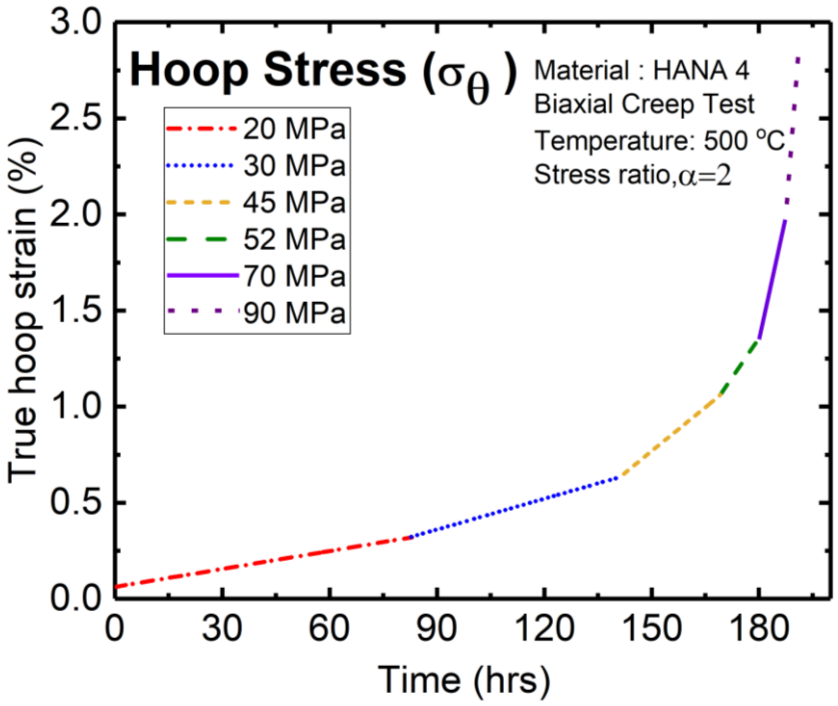

Figure 5.5. Creep curves from biaxial creep test of HANA 4 at 500^0C at stress ratio of 2.

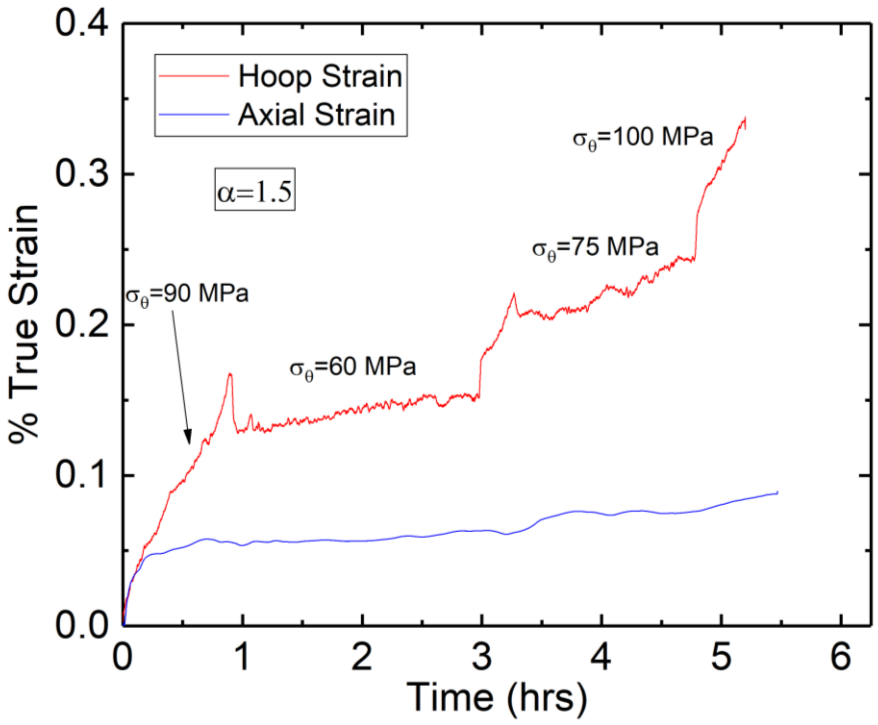

Figure 5.6. Creep curves from biaxial creep test of HANA 4 at 500^0C at stress ratio of 1.5.

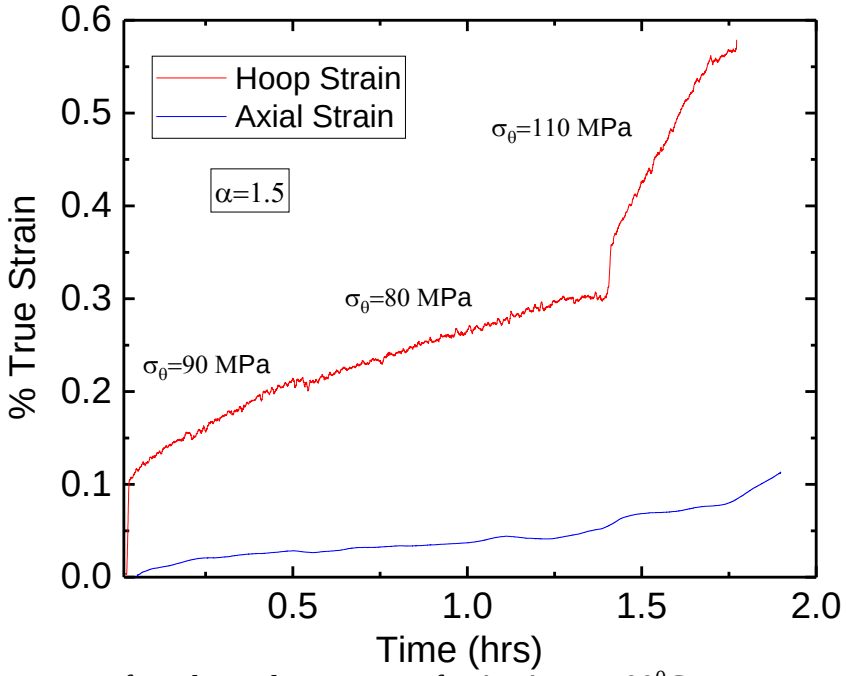

Figure 5.7. Creep curves from biaxial creep test of HANA 4 at 500^0C at stress ratio of 1.5.

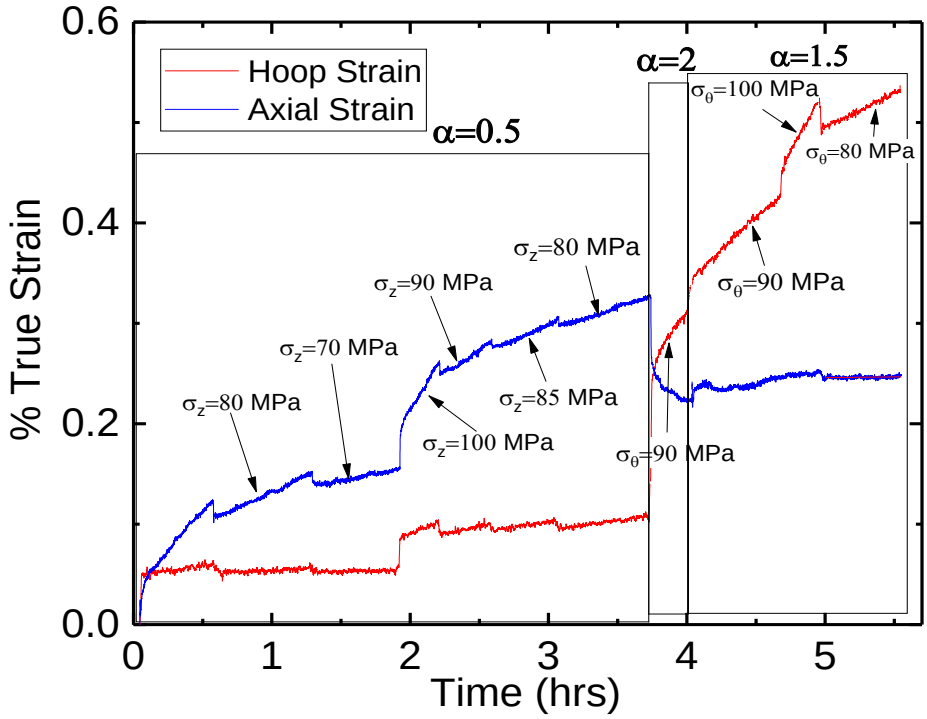

Figure 5.8. Creep curves from biaxial creep test of HANA 4 at 500^0C at various stresses and stress ratios.

Finally, a creep test was performed at different stress ratios at different stresses in a random order on the same sample to verify the previous results and to get error bars in the strain rate these curves are depicted in Figure 5. 8.

5.2. Evaluation of Creep Anisotropy Parameters

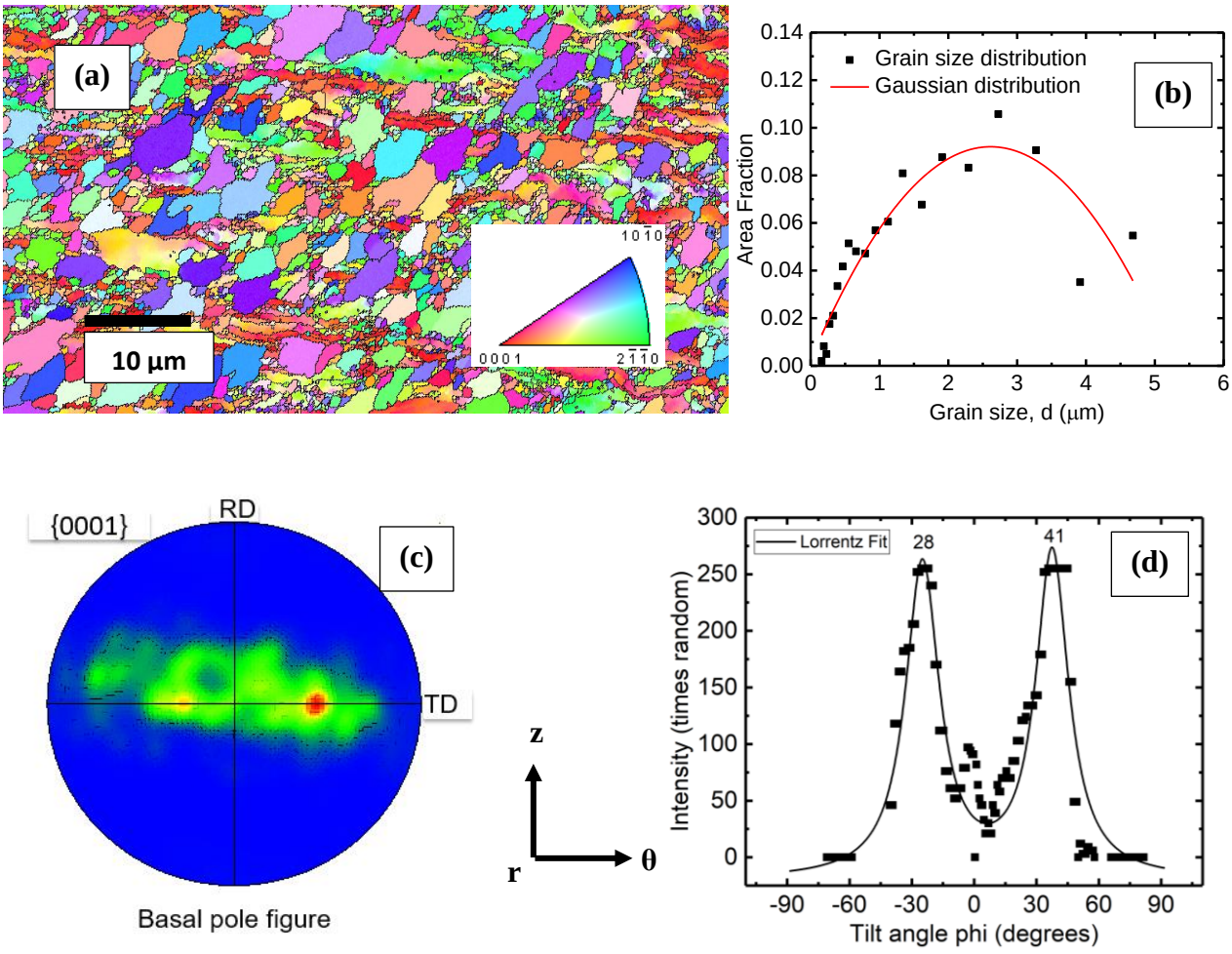

Figure 5.9. a. EBSD Micrograph, b. Grain size distribution in CWSR condition, c. {0002} basal pole figure and d. intensity vs angle for basal pole peak angle determination.

Fig. 5.9 (a) shows the EBSD micrograph in axial-hoop (z-θ) plane. Clearly, the grains are not very highly elongated which is surprising because Murty et al [23] have reported a very high degree of elongation in CWSR Zircaloy-4 grains along both the radial-axial and hoop-axial plane, none of

which is observed in CWSR HANA-4. The grain size distribution along axial-hoop plane shown in Fig. 5.9(b). The maximum area fraction is found to be at a grain size of around 2.5 μm. Basal pole figure is shown in Fig. 5.9(c) the basal pole peak angle which is the average angle along which basal poles are located is found to be asymmetric (the regions are shown in red) which is rare and the reason of it is not clearly understood.

To get the R-value from the basal pole figure following equation was used,

$$R=\cot^2\bar{\varphi} \tag{5.1}$$

Where $\bar{\varphi}$=angle between the radial direction and the c-axis of the average crystal in the r-θ plane

From Figure 5.9 (c) it is observed that one side of the pole has more intensity than the other. The basal peak pole angle then was computed as follows:

$\bar{\varphi}$= φ_1 *normalized pole1 intensity + φ_2*normalized pole2 intensity

Which yielded $\bar{\varphi} = \pm 38 \pm 3^0$

$R = 1.6 \pm 0.79$

Figure 5.9 depicts ρ versus α curve which was obtained from current experiments. It can be shown that $\alpha_{(\rho=0)} = \frac{P}{1-P}$ from which P can be evaluated.

For equi-biaxial loading α=1,

$$\beta = \left(\frac{\dot{\varepsilon}_\theta}{\dot{\varepsilon}_r}\right)_{\alpha=1} = \left(\frac{R}{P}\right)_{\alpha=1} \tag{5.2}$$

After R&P are known, a curve can be drawn such that it passes through the experimental data points and matches with the obtained R&P values.

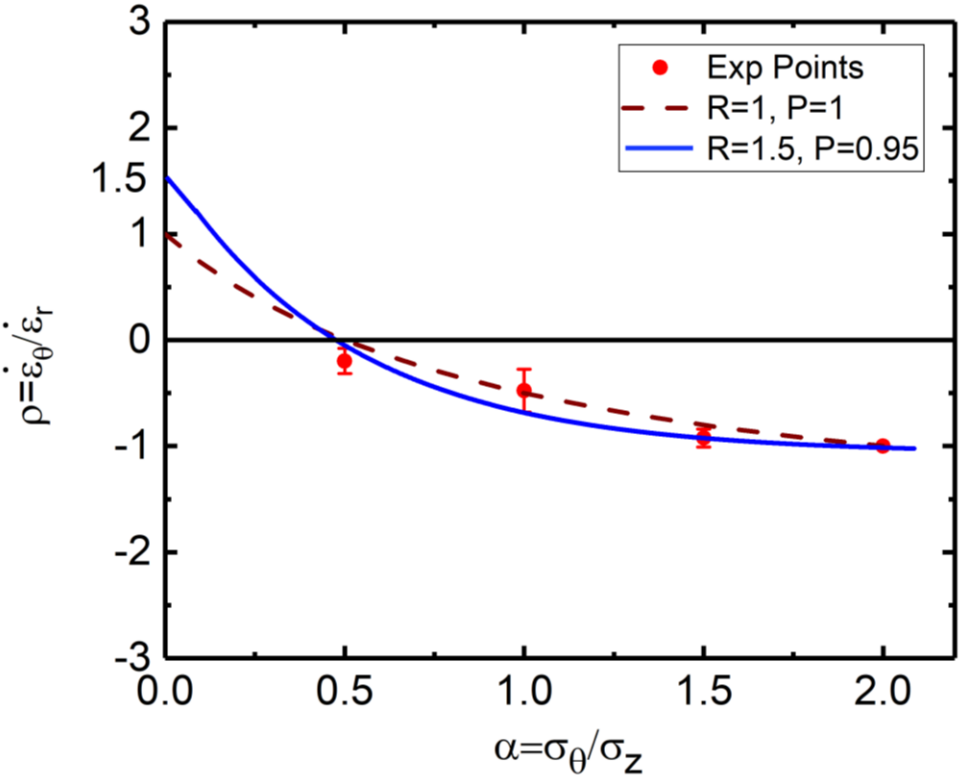

Figure 5.10. Strain-rate ratio versus stress ratio for biaxial creep of HANA-4 alloy.

5.3. Creep loci of HANA-4

Work dissipation energy (Ẇ) is given by:

$$\dot{W} = \sigma_z \dot{\epsilon}_z + \sigma_\theta \dot{\epsilon}_\theta \quad (5.3)$$

Table 5.1 summarizes the creep rates obtained during biaxial creep tests of HANA-4 along with the calculated work dissipation energy for the same.

Using equation 5.3, the plot of $\dot{W}$ vs σ_z was plotted for various stress ratios. A creep loci was generated using $\dot{W} = 20\ \frac{J}{m^3 s}$. As seen in Figure 5. 11 curves corresponding to different loading conditions are parallel to each other.

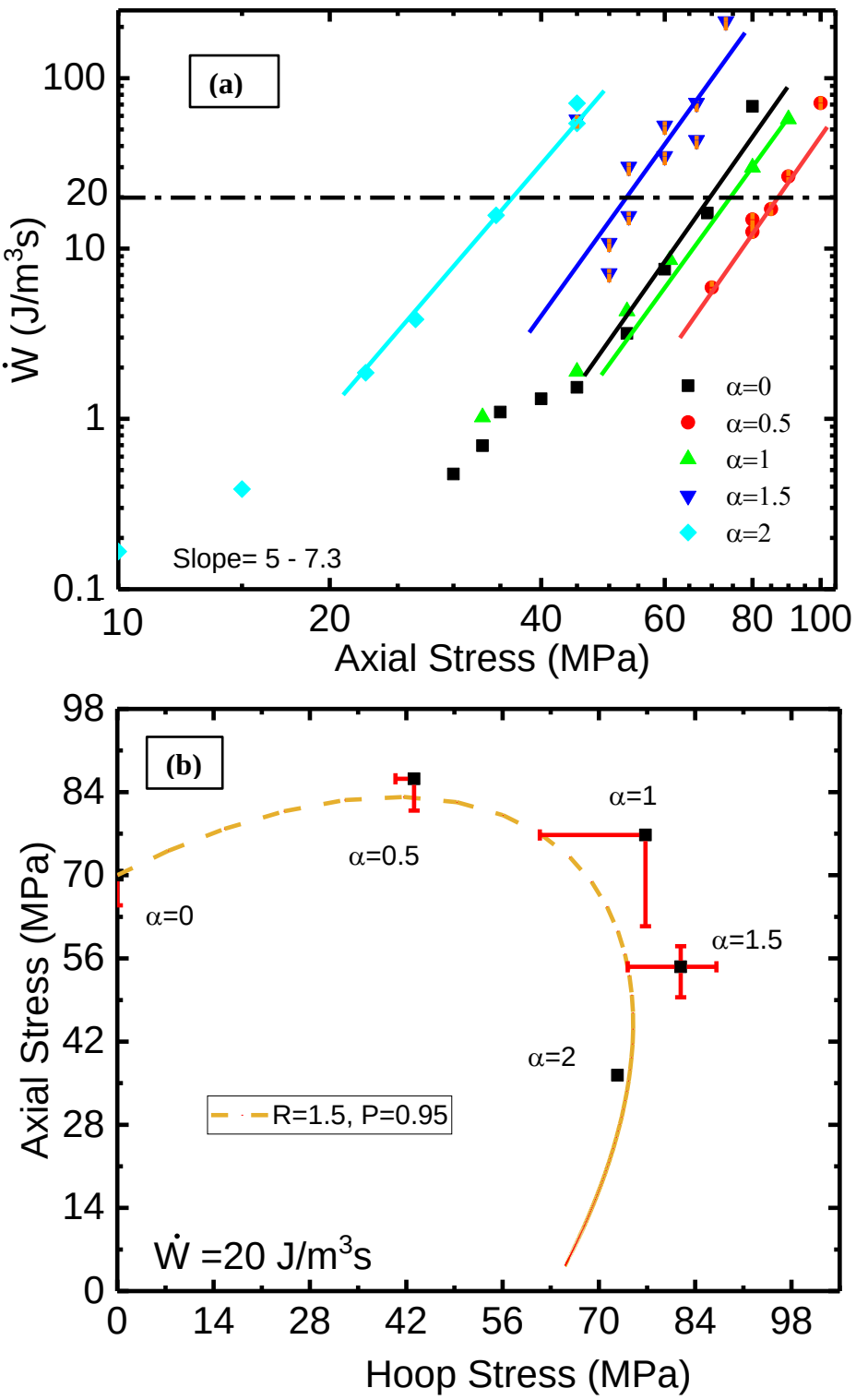

Figure 5.11. Plot of (a): Work dissipation rate vs Axial Stress (b): Creep Loci at constant work dissipation rate.

Table 5.1. Summary of the creep rates obtained from biaxial creep tests of HANA-4 from stress ratio of 0-2 at various stresses

α	σ_z (MPa)	σ_θ (MPa)	$\dot{\varepsilon}_\theta$ (s^{-1})	$\dot{\varepsilon}_z$ (s^{-1})	$\frac{\dot{\varepsilon}_\theta}{\dot{\varepsilon}_z}$	$\dot{W}$ (J/m^3s)
0	0	30	0	1.58E-08	0	0.47
0	0	33	0	2.11E-08	0	0.70
0	0	35	0	3.13E-08	0	1.09
0	0	40	0	3.28E-08	0	1.31
0	0	45	0	3.40E-08	0	1.53
0	0	53	0	5.98E-08	0	3.17
0	0	60	0	1.26E-07	0	7.56
0	0	69	0	2.34E-07	0	16.15
0	0	80	0	8.54E-07	0	68.32
0.5	40	80	1.52E-08	1.77E-07	0	14.77
0.5	40	80	5.10E-08	1.31E-07	0	12.52
0.5	35	70	8.37E-09	8.00E-08	0	5.89

Table 5.1 (continued).

0.5	42.5	85	6.27E-08	1.69E-07	0	17.03
0.5	45	90	8.76E-08	2.50E-07	0	26.44
0.5	50	100	1.58E-07	6.35E-07	0	71.40
1	33	33	8.53E-09	2.25E-08	0.38	1.02
1	45	45	1.95E-08	2.26E-08	0.86	1.89
1	53	53	4.05E-08	4.04E-08	1.00	4.29
1	61	61	7.47E-08	6.60E-08	1.13	8.58
1	80	80	1.85E-07	1.89E-07	0.98	29.91
1	90	90	3.82E-07	2.57E-07	1.49	57.51
1.5	90	60	5.73E-07	1.70E-08	33.71	52.59
1.5	90	60	3.54E-07	4.95E-08	7.15	34.83
1.5	80	53.33	3.34E-07	6.47E-08	5.16	30.17
1.5	80	53.33	1.89E-07	6.65E-09	28.42	15.47

Table 5.1 (continued).

1.5	75	50	9.37E-08	2.50E-09	37.48	7.15
1.5	75	50	1.39E-07	7.00E-09	19.86	10.78
1.5	100	66.6	4.02E-07	4.60E-08	8.74	43.26
1.5	100	66.6	6.89E-07	3.98E-08	17.30	71.55
1.5	110	73.3	1.88E-06	1.22E-07	15.41	215.74
2	20	10	8.32E-09	0		0.17
2	30	15	1.29E-08	0		0.39
2	45	22.5	4.14E-08	0		1.86
2	53	26.5	7.24E-08	0		3.84
2	69	34.5	2.27E-07	0		15.66
2	90	45	6.03E-07	0		54.27
2	90	45	7.91E-07	0		71.19
2	90	45	5.89E-07	8.95E-08	6.58	57.04

5.4. Comparison of current experimental creep results with other alloys

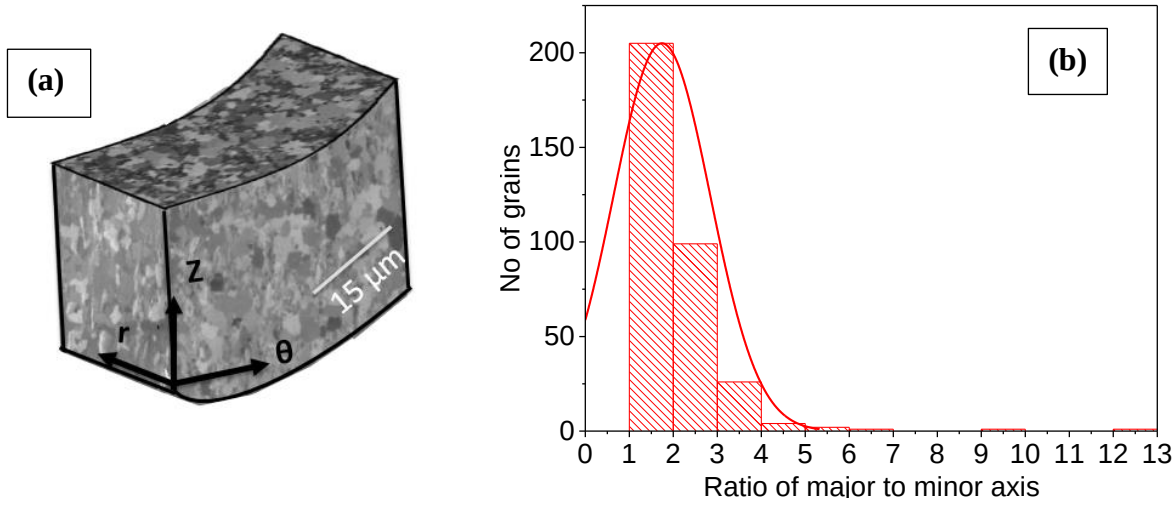

Figure. 5.12 a. SEM micrograph, b. Quantitative measure of elongated grains in r-z plane for as-received HANA-4.

Fig. 5.12 (a) depicts the tube microstructure. The grains were first subjected to FIB in an SEM. Since each grain has a different orientation relative to the other the etching rate was different for each grain. The contrast generated due to this made it possible to examine the grains under SEM.

The grains in the axial-radial plane are elongated along the axial direction. This is expected since the tube is in cold-worked condition. It was of interest to measure this degree of elongation which was measured using Image J software where each grain was assumed elliptical. The result is shown in Fig. 5.12 (b). Maximum number of grains showed the degree of elongation which is defined as the ratio of major to minor axis of the ellipse close to 1.8 which is not substantially high and for practical purposes, the grain shape is closer to equiaxed than columnar.

Figure 5.13 shows a comparison of creep loci of CWSR HANA-4 with Rx (Recrystallised)-HANA 4 and CWSR-Zircaloy-4. The creep loci of both CWSR and Rx-HANA 4 show a very slight deviation from creep loci of isotropic material. CWSR Zircaloy-4 is highly anisotropic

compared to HANA-4. From the following observations, it can be concluded that creep loci of HANA-4 doesn't depend on initial state (CWSR or Rx) which is quite unique considering the same doesn't apply for Zircaloy and ZIRLO®. Murty et al have shown that grain shape anisotropy is a major factor responsible for the change in creep loci in CWSR material. In Zircaloy and ZIRLO® CWSR is known to produce elongated grains along the axial direction. From the present study, it is postulated that the same is not true for HANA-4 and is thought to be the reason for its close to isotropic behavior.

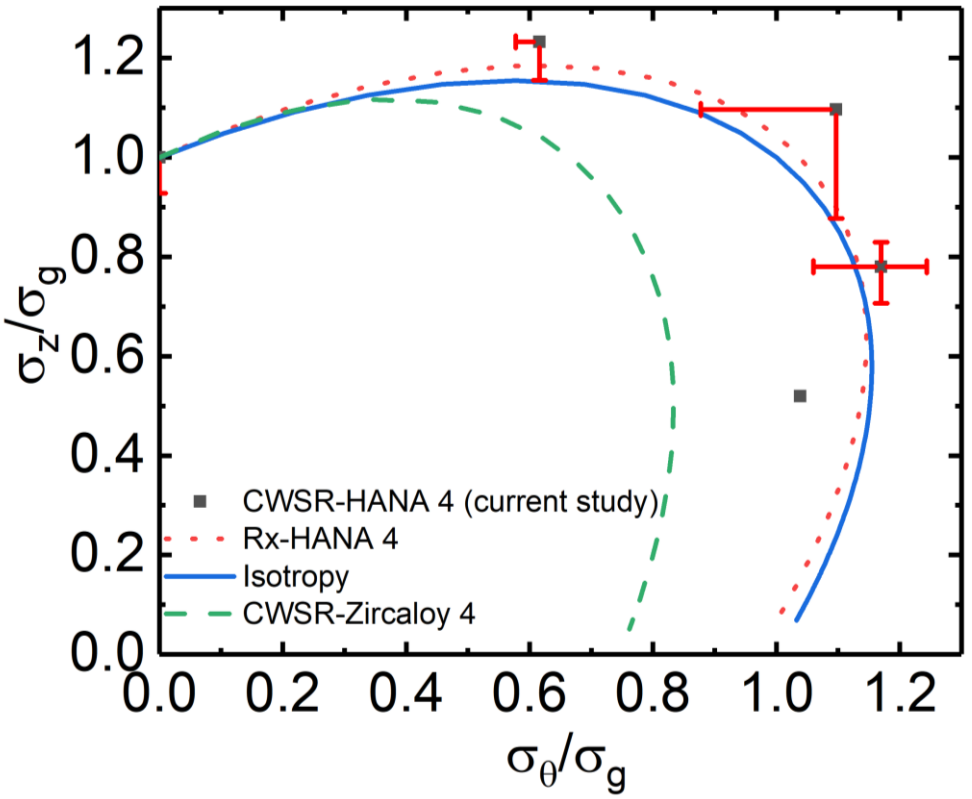

Figure 5. 13. Comparison of creep loci of CWSR Zircaloy-4, Rx and CWSR HANA-4.

5.5 Prediction of the active slip system

With n=5, a creep locus was predicted for CWSR HANA-4 as shown in Fig.11.

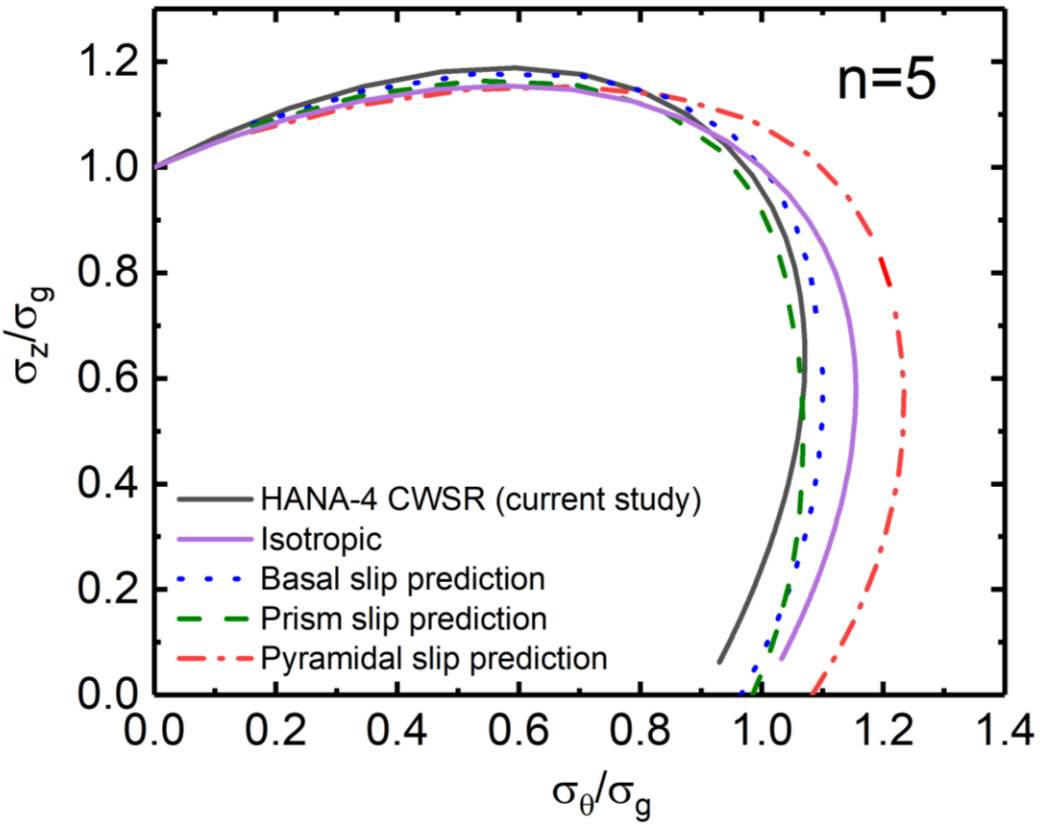

Figure 5. 14. Creep Loci of CWSR HANA-4 with model prediction assuming prismatic or basal slip.

Table 5.2-Summary of R & P values obtained.

Type	**Slip System**	**R**	**P**	**R/P**
Experimental	By fitting & EBSD	1.5	0.95	1.58
	Creep test , $\alpha = 1$			1.25 ± 0.25
Simulation	Prism	1.24	0.66	1.87
	Basal	1.37	0.98	1.4
	Pyramidal	0.932	1.293	0.72

From Fig. 5.14 it is observed that both the basal slip and prismatic slip prediction lie close to the predicted creep loci for CWSR HANA-4. Table 5.2 summarizes R&P values obtained for

basal and prismatic slip prediction as well as the one that was obtained experimentally. The c/a ratio of Zr alloys is 1.593 which is less than the ideal value of 1.63, the possible slip systems in hcp materials are prism, basal and prismatic. It is well known for Zr that basal slip is dominant at low temperatures and high strain rates. Also, at high-temperatures basal slip is easily activated in pure Zr. Akhtar observed basal slip in pure Zr single crystals above 577 ^{0}C [13]. One study on Zircaloy-2 found that the basal slip was relatively easily activated at room temperature and low strain rates [14]. In previous studies conducted by Murty et al on CWSR Zircaloy-4 at 400-500 ^{0}C basal slip prediction using CODF was found to show a better match with the experimental results. It was thought that in CWSR material the prismatic planes are locked due to high deformation leading to activation of basal slip systems [52]. This was proven to be not true after TEM analysis. So, to explain the deviation of prismatic slip prediction from the experimental results a model was introduced by Murty et al which assumed grain boundary sliding mechanism along the hoop and radial direction (due to elongated grains along axial direction) with the combination of prismatic slip. This model showed excellent agreement with the experimental results it is interesting to note that the aspect ratio of grains in CWSR HANA-4 along the axial direction is not that high based on the figure.5.12 (b) and the creep locus is closer to that of an isotropic material, so grain boundary sliding mechanism is not expected to occur.

In this case, considering only basal, prismatic or combination of both slip systems can explain the results well. But, it is difficult to exactly predict the active slip system under current experimental conditions. Although it is worth noting that basal prediction showed closer correspondence than prismatic slip to experimental results. Further, microstructural evidence is necessary to find out the active slip system.

FeCrAl

5.6. Stress vs rupture time

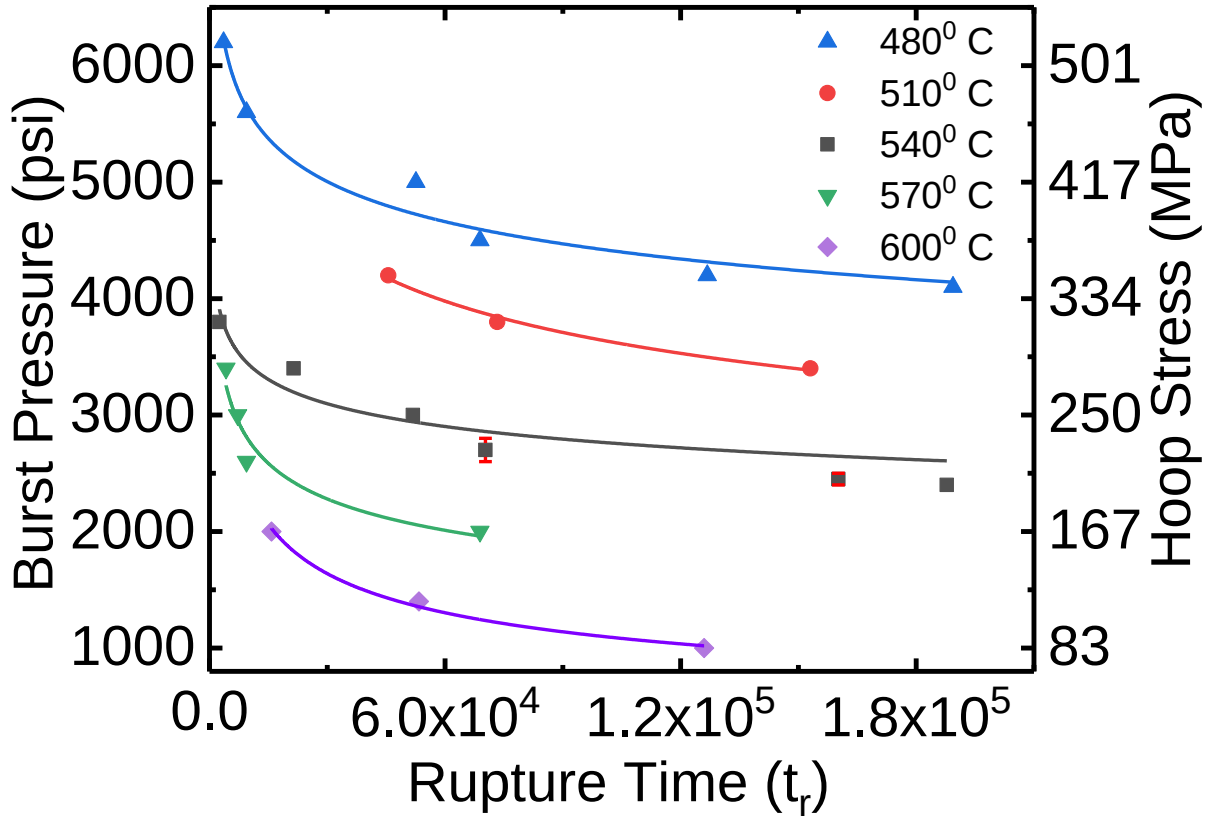

Figure 5.15. Plot depicting stress against rupture time for various temperatures

Figure 5.15 shows the effect of stress on rupture time at temperatures of 480, 510, 540,570 and 600 ^{0}C respectively. To convert pressure in psi to hoop stress in MPa the multiplying factor of 11.98 has been used. As expected the rupture time decays exponentially with decreasing stress.

5.7. Monkmann-Grant relation

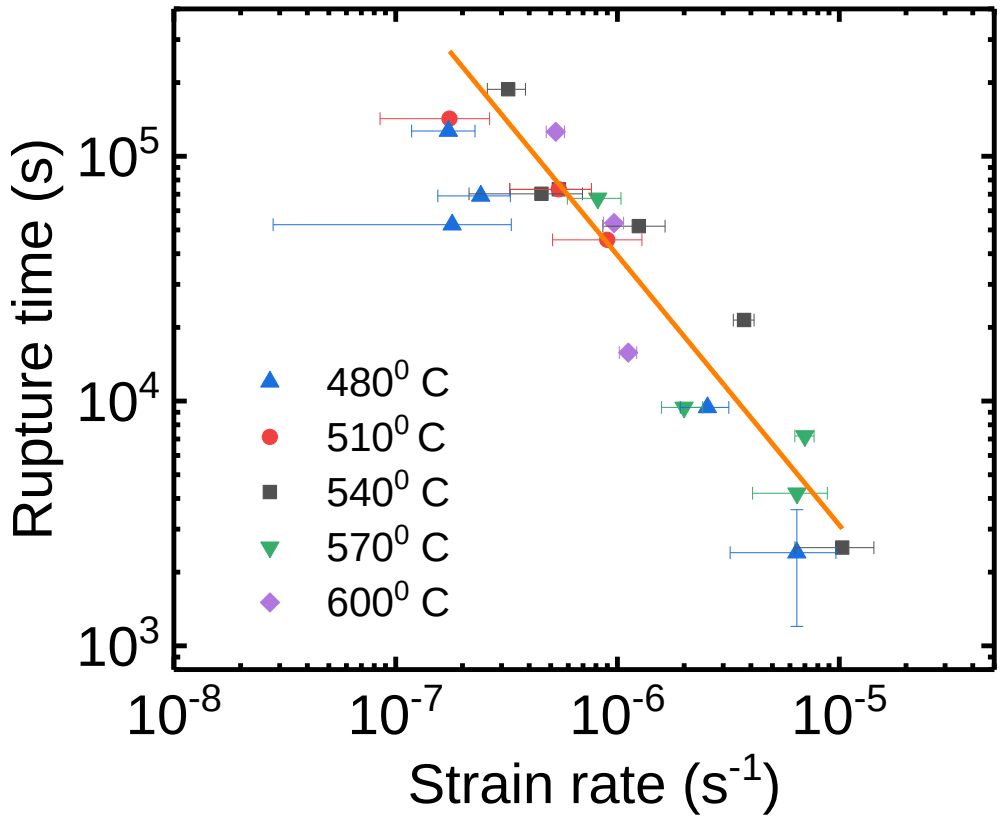

Figure 5.16. Plot depicting the agreement of Monkman-Grant Relation.

Fig. 5.16 shows that FeCrAl-C26M2 satisfies Monkman-Grant relationship. The exact relation between rupture time and strain rate for C26M2 is shown in Equation (5).

$$\dot{\varepsilon} t_r = K = 0.03 \pm 0.027 \quad (5.4)$$

As visible, the scatter in the data is pretty large. Monkman and Grant [53] have reported similar scatter for ferritic steels containing upto 13 % Cr in the temperature range of 427-704^0 C [54]. In this study, a correlation between scatter and fracture mode was observed. The points which lie on the left side of the fitting line, those samples failed by direct open-up whereas those lying on the right of or on the fitting line failed by small crack-hole type fracture both of these fracture modes are depicted in section 5.11.

5.8. Larson-Miller Parameter

The Larson-Miller Parameter (LMP) [55] was calculated using the equation

$$P=T(\log_{10} t_r + C) \quad (5.5)$$

Where T is the temperature in ^{o}K, t_r is rupture time in hrs and C is 20.

Values of LMP were obtained for various stresses at various temperatures and equation (5.6) was obtained using fitting a line through those points.

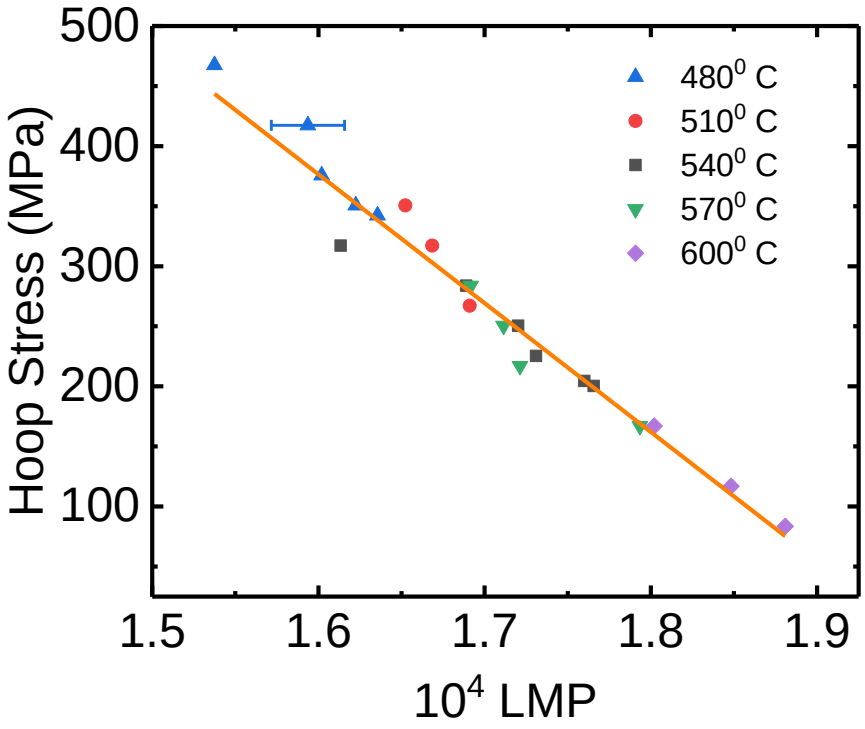

Figure 5.17. Effect of stress on Larson Miller Parameter.

A linear relationship was found between stress and Larson-Miller Parameter:

$$\sigma(MPa) = [-(0.1) \times (LMP)] + (2092 \pm 75) \quad (5.6)$$

5.9. Activation Energy

Creep rate is given by:

$$\dot{\varepsilon} = Aexp(\frac{Q}{RT})\sigma^{n} \quad (5.7)$$

Where A is a function of σ/E, Q is the activation energy and n is the stress exponent.

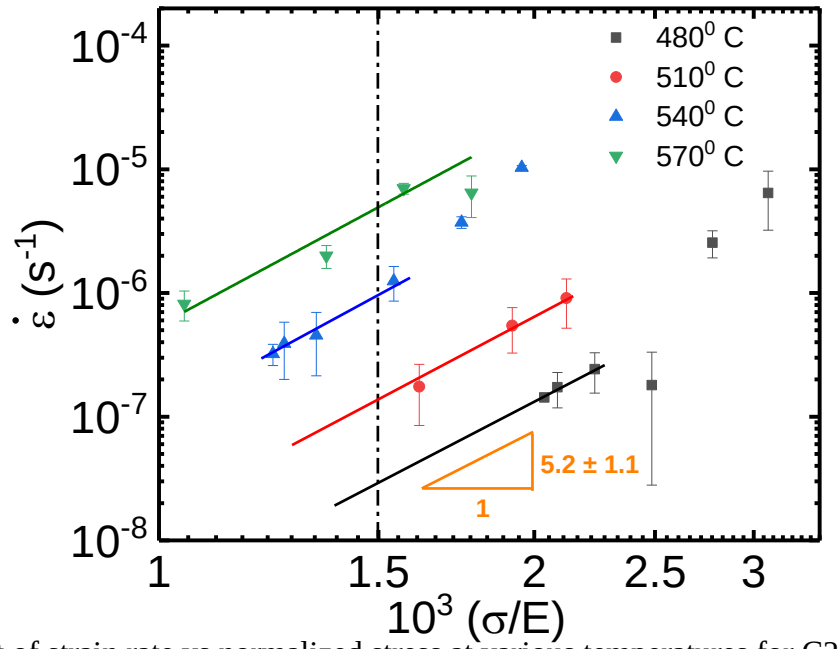

Figure 5.18. Plot of strain rate vs normalized stress at various temperatures for C26M2-FeCrAl in temperature range of 480-570 ^{0}C.

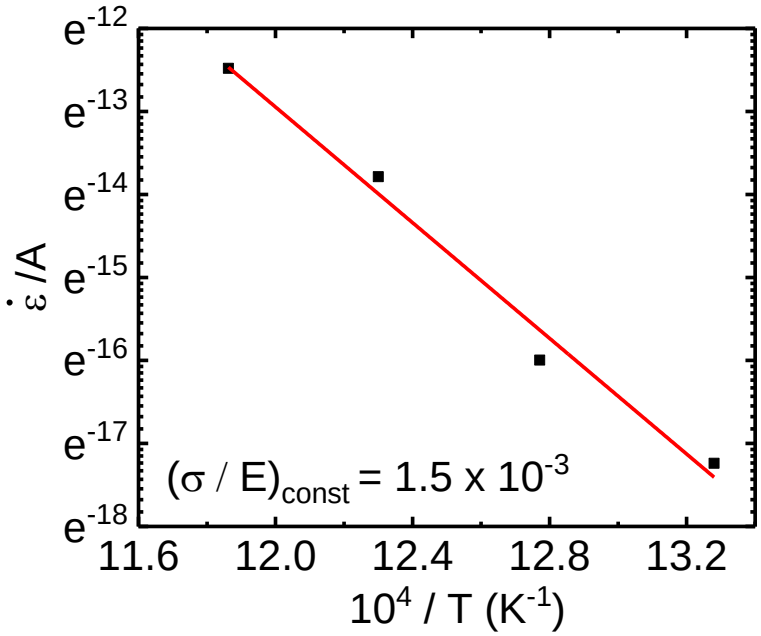

Figure 5.19. Plot depicting determination of activation energy at constant normalized stress

As shown in Figure 5.19 at constant $\frac{\sigma}{E}$ of 1.5 x 10^{-3} plotting strain rate vs 1/T yielded activation energy (Q) of 289 $\pm$ 25 kJ/mol. The activation energy of self-diffusion of Fe in bcc Fe is 251 kJ/mol [56] and is in close agreement with the obtained value.

5.10. BMD plot

The diffusion coefficient is given by

$$D=D_0\exp\left(\frac{-Q}{RT}\right) \quad (5.9)$$

The obtained value of Q was used to calculate diffusivity. Value of D_0 was taken as 2.8 x 10^{-4} m/s^2 and b as 3.1 x 10^{-10} m.

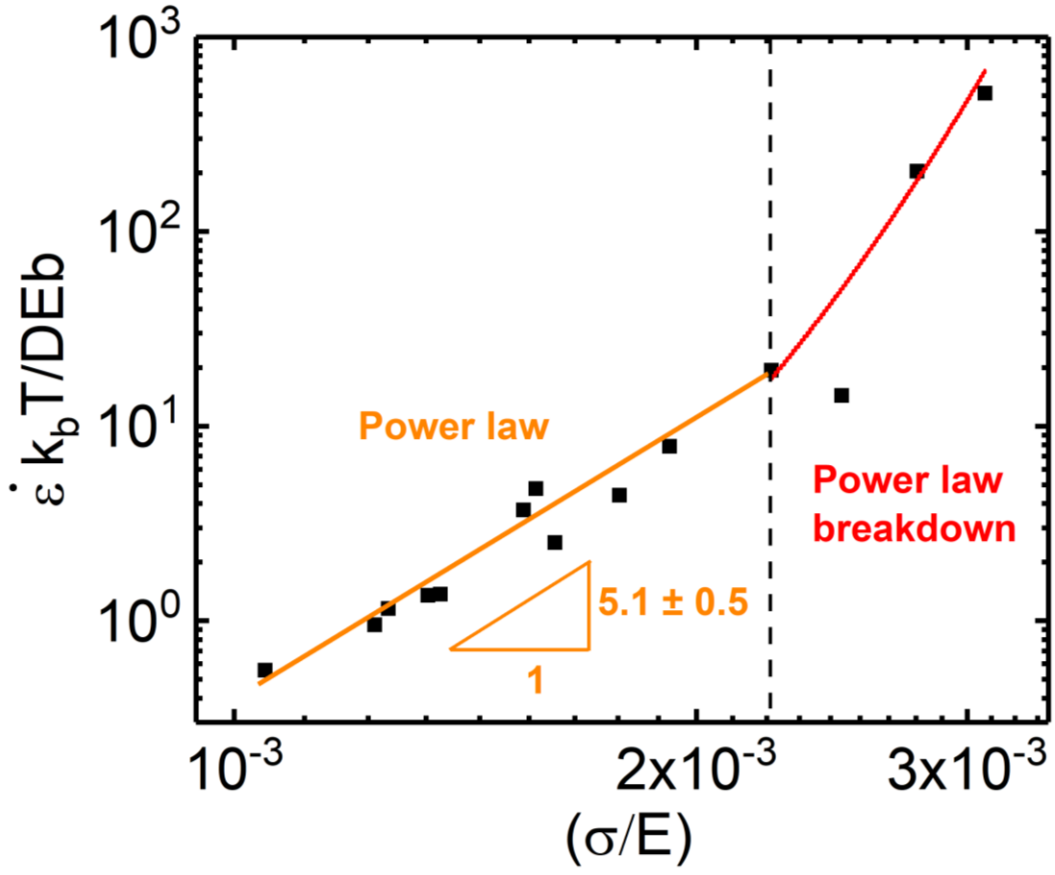

Figure 5.20. BMD relation for C26M2 in temperature range of 480-570 ^{0}C.

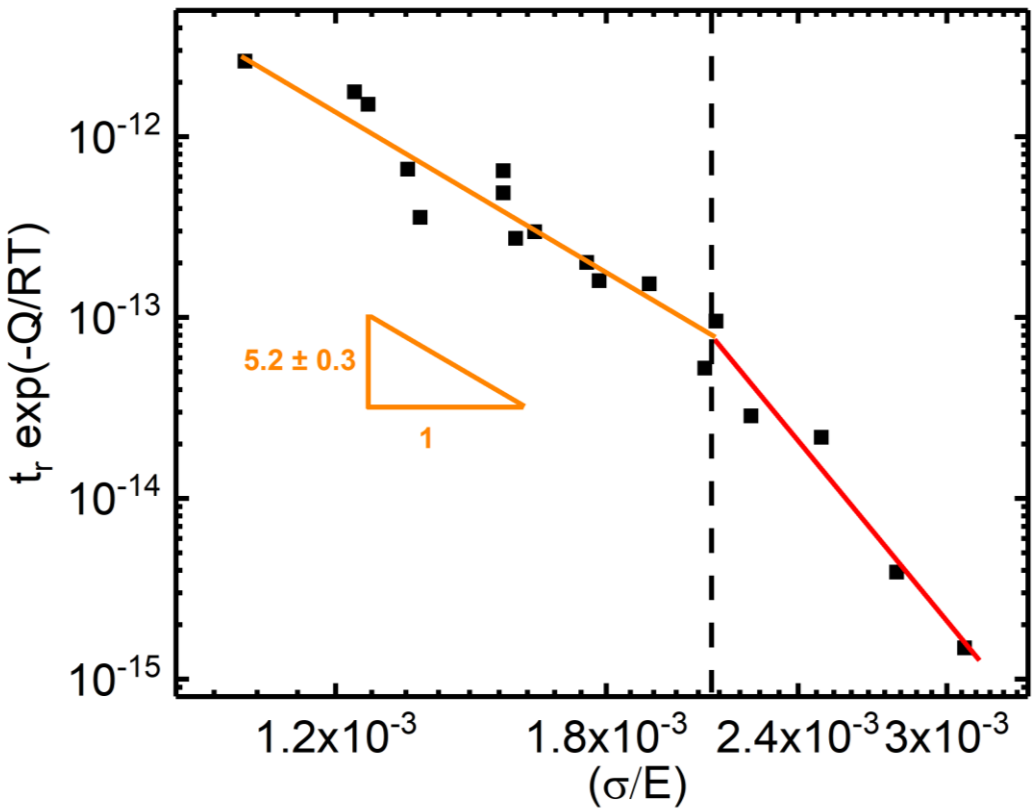

Figure 5.21. A plot of normalized time against normalized stress illustrating a transition in creep mechanism in temperature range of 480-570 ^{0}C.

It is evident that the three high-stress points at 650^0 C fall in power-law break down (PLB) region

Expressed by equation

$$\frac{\dot{\varepsilon} kT}{DEb} = 7.63 \times 10^{-4} \exp\left(4355 \frac{\sigma}{E}\right) \quad (5.10)$$

Table 5.2. Summary of creep data obtained from experiments.

Material	Cr,Al (wt%)	Temp Range (^{0}C)	n	Q (kJ/mol)	Stress regime (MPa)
C26M2	12,6	480-570	5.1±0.5	289±25	170-376

5.11. Microstructural features of the samples

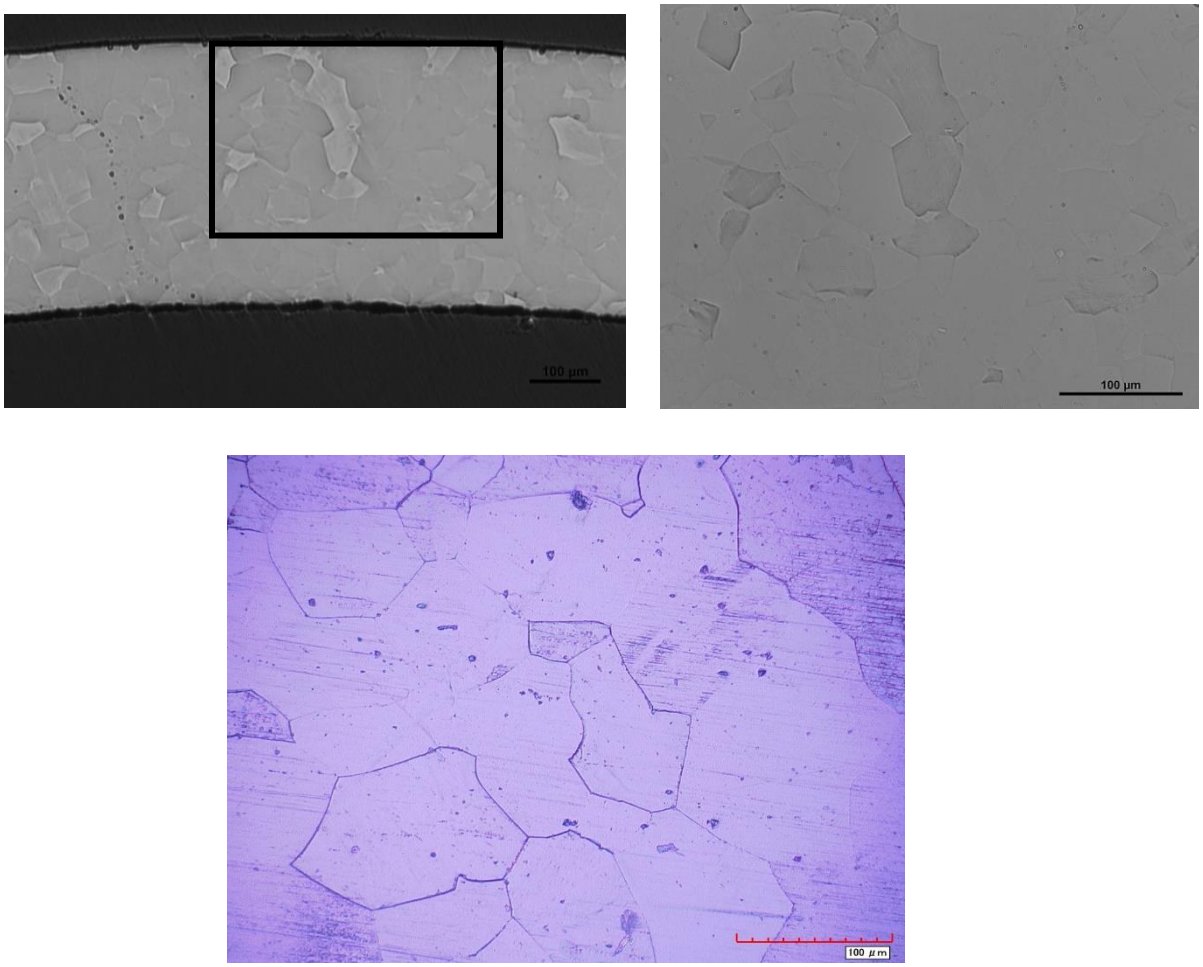

Figure 5.22 Optical Micrograph of a,b) FeCrAl-C26M2 (courtesy: ORNL) c) FeCrAl- B136Y.

The grain size of the as-received material was found to lie between 50-75µm.

Figure 5.23. Typical burst test specimens (a) direct open-up, (b) small crack and hole opening.

Two fracture modes were visible after the burst test. It is suspected that the fracture by small crack formation (or hole formation) occurs at high temperature and low stresses and open up fracture occurs at low temperature and high stresses. This was observed but there were some exceptions hence this just remains an assertion and not a conclusion. The crack formation might be due to the intergranular void formation which needs to be confirmed by SEM/TEM.

5.12 Summary of Burst Test results

The creep properties of FeCrAl tubing were studied by employing the burst testing technique. The rupture data were fit to both the empirical relations, Larson–Miller parameter and Monkman–Grant. The scatter in the Monkman-Grant relation was correlated with the change in fracture mechanism. The strain-rates versus normalized (through temperature-dependent elastic modulus) stress gave activation Energy (Q_c) of 289$\pm$ 25 kJ/mol. Two distinct regions (Power Law and PLB) were obtained in the BMD plot. In the temperature range of 480-570 ^{0} C, the slope of

power law region indicated an n-value close to 5 suggesting dislocation climb as the main creep mechanism. A sharp change in BMD plot reveals the inherent dangers involved in the blind extrapolation of short-term (high temperature and high stress) data to in-service conditions of low temperatures/stresses. As shown in the previous study [57] for Ti, the burst testing was established successfully used for evaluating the creep properties of FeCrAl-C26M2.

ACKNOWLEDGEMENTS

The author acknowledges the use of the Analytical Instrumentation Facility (AIF) at North Carolina State University, which is supported by the State of North Carolina and the National Science Foundation. This work is supported by National Science Foundation through grant CMMI-1727237.

REFERENCES

[1] T.G. Langdon, An analysis of flow mechanisms in high temperature creep and superplasticity, Materials transactions. 46 (2005) 1951-1956.

[2] R.S. Ghosh, J. Timusk, Creep of Portland cement paste at sub-zero temperature, Matériaux et constructions. 4 (1971) 171-176.

[3] J.E. Bird, A.K. Mukherjee, J.E. Dorn, Correlations between high-temperature creep behavior and structure, (1969).

[4] B. Kombaiah, Transitions in Creep Mechanisms of Zirconium Alloys, PhD dissertation, 2015

[5] J. Weertman, Steady-state creep of crystals, J. Appl. Phys. 28 (1957) 1185-1189.

[6] J. Poirier, Creep of Crystals: High-Temperature Deformation Processes in Metals, Ceramics and Minerals, Cambridge University Press, 1985.

[7] B.W. Marple, Creep-Rupture Study of Annealed Zircaloy 4: Stress and Temperature Effects, (2005).

[8] J. Weertman, Theory of steady-state creep based on dislocation climb, J. Appl. Phys. 26 (1955) 1213-1217.

[9] D.G. Franklin, G.E. Lucas, A.L. Bement, Creep of Zirconium Alloys in Nuclear Reactors, ASTM International, 1983.

[10] A.K. Mukherjee, The rate controlling mechanism in superplasticity, Materials Science and Engineering. 8 (1971) 83-89.

[11] E. Tenckhoff, Deformation Mechanisms, Texture, and Anisotropy in Zirconium and Zircaloy, ASTM International, 1988.

[12] G.G. Yapici, C.N. Tomé, I.J. Beyerlein, I. Karaman, S.C. Vogel, C. Liu, Plastic flow anisotropy of pure zirconium after severe plastic deformation at room temperature, Acta Materialia. 57 (2009) 4855-4865.

[13] A. Akhtar, Basal slip in zirconium, Acta metallurgica. 21 (1973) 1-11.

[14] H. Qiao, P.D. Wu, H. Wang, M.A. Gharghouri, M.R. Daymond, Evaluation of elastic–viscoplastic self-consistent polycrystal plasticity models for zirconium alloys, Int. J. Solids Structures. 71 (2015) 308-322.

[15] A.T. Motta, A. Couet, R.J. Comstock, Corrosion of zirconium alloys used for nuclear fuel cladding, Annual Review of Materials Research. 45 (2015) 311-343.

[16] S. Park, M. Lee, B. Choi, J. Baek, J. Park, J. Kim, H. Kim, Out-of-pile and In-pile Perfomance of Advanded Zirconium Alloys (HANA) for High Burn-up Fuel AU - JEONG, Yong Hwan, J Nucl Sci Technol. 43 (2006) 977-983.

[17] Creep Behavior of Niobium Containing Zirconium Alloys – an Overview, SMIRT-19 conference, 2007

[18] Z. Duan, H. Yang, Y. Satoh, K. Murakami, S. Kano, Z. Zhao, J. Shen, H. Abe, Current status of materials development of nuclear fuel cladding tubes for light water reactors, Nucl. Eng. Des. 316 (2017) 131-150.

[19] Duncombe E, Freidrich C.M, Guilliner W.H, An analytical model for the prediction of In-pile behavior of oxide fuel rods, Nuclear technology. 12 (1971) 194.

[20] I. Charit, K. Linga Murty, Texture and creep anisotropy in zirconium alloys, 539 (2007) 3377-3382.

[21] K.L. Murty, I. Charit, Texture development and anisotropic deformation of zircaloys, Prog. Nuclear Energy. 48 (2006) 325-359.

[22] N. Kumar, K. Grundy, B. Kombaiah, B. Luan, K. Murty, Anisotropic Biaxial Creep of Textured Nb-Modified Zircaloy-4 Tubing, (2017) 19-32.

[23] K.L. Murty, B.V. Tanikella, J.C. Earthman, Effect of grain shape and texture on equi-biaxial creep of stress relieved and recrystallized Zircaloy-4, Acta metallurgica et materialia. 42 (1994) 3653-3661.

[24] Fukushima Daiichi Accident, www.world-nuclear.org/Information-Library/Safety-and-Security/Safety-of-Plants/Fukushima-Accident.aspx , (2019).

[25] IAEA, Review of Fuel Failures in Water Cooled Reactors., Nucl. Energy Ser. NF-T-2.1, IAEA, Vienna, Austria, 2010.

[26] J.K. Shultis, R.E. Faw, Fundamentals of Nuclear Science and Engineering Third Edition, CRC press, 2016.

[27] K. Terrani, Accident tolerant fuel cladding development: Promise, status, and challenges, J. Nucl. Mater. (2018).

[28] J.J. Powers, A. Worrall, K.R. Robb, N.M. George, G.I. Maldonado, ORNL Analysis of Operational and Safety Performance for Candidate Accident Tolerant Fuel and Cladding Concepts, IAEA TECDOC SERIES. (2016) 253.

[29] Y. Katoh, L.L. Snead, I. Szlufarska, W.J. Weber, Radiation effects in SiC for nuclear structural applications, Current Opinion in Solid State and Materials Science. 16 (2012) 143-152.

[30] M. Ben-Belgacem, V. Richet, K.A. Terrani, Y. Katoh, L.L. Snead, Thermo-mechanical analysis of LWR SiC/SiC composite cladding, J. Nucl. Mater. 447 (2014) 125-142.

[31] Z. Karoutas, J. Brown, A. Atwood, L. Hallstadius, E. Lahoda, S. Ray, J. Bradfute, The maturing of nuclear fuel: Past to Accident Tolerant Fuel, Prog. Nuclear Energy. 102 (2018) 68-78.

[32] R.T. Sweet, Thermo-mechanical analysis of iron-chromium-aluminum (FeCrAl) alloy cladding for light water reactor fuel elements, (2018).

[33] A. Strasser, J. Santucci, K. Lindquist, W. Yario, G. Stern, L. Goldstein, L. Joseph, Evaluation of stainless steel cladding for use in current design LWRs.Final report. (1982).

[34] KANTHAL, https://www.kanthal.com/en/about-us/, 2017.

[35] G. Bonny, D. Terentyev, L. Malerba, on the α–α′ miscibility gap of Fe–Cr alloys, Scr. Mater. 59 (2008) 1193-1196.

[36] A. Hishinuma, S. Isozaki, S. Takaki, K. Abiko, Attractive Characteristics of High-Chromium Iron-Based Alloys for Nuclear Reactor Application, physica status solidi (a). 160 (1997) 431-440.

[37] H. Kim, H. Kim, J. Yang, Y. Koo, On the Minimum Thickness of FeCrAl Cladding for Accident-Tolerant Fuel, Nucl Technol. 198 (2017) 342-346.

[38] R.B. Rebak, K.A. Terrani, W.P. Gassmann, J.B. Williams, K.L. Ledford, Improving nuclear power plant safety with FeCrAl alloy fuel cladding, MRS Advances. 2 (2017) 1217-1224.

[39] C.P. Massey, P.D. Edmondson, K.G. Field, D.T. Hoelzer, S.N. Dryepondt, K.A. Terrani, S.J. Zinkle, Post irradiation examination of nanoprecipitate stability and α′ precipitation in an oxide dispersion strengthened Fe-12Cr-5Al alloy, Scr. Mater. 162 (2019) 94-98.

[40] R.B. Rebak, Versatile oxide films protect FeCrAl alloys under normal operation and accident conditions in light water power reactors, JOM. 70 (2018) 176-185.

[41] J. Engkvist, U. Bexell, M. Grehk, M. Olsson, High temperature oxidation of FeCrAl-alloys–influence of Al-concentration on oxide layer characteristics, Materials and corrosion. 60 (2009) 876-881.

[42] Y. Yamamoto, Z. Sun, B.A. Pint, K.A. Terrani, Optimized Gen-II FeCrAl cladding production in large quantity for campaign testing, Oak Ridge: Oak Ridge National Laboratory. (2016).

[43] C.P. Massey, K.A. Terrani, S.N. Dryepondt, B.A. Pint, Cladding burst behavior of Fe-based alloys under LOCA, J. Nucl. Mater. 470 (2016) 128-138.

[44] C.S. Wukusick, J.F. Collins, An iron-chromium-aluminum alloy containing yttrium, Mater.Res.Std. 4 (1964).

[45] J.D. Whittenberger, Tensile and creep properties of the experimental oxide dispersion strengthened iron-base sheet alloy MA-956E at 1365 K, Metallurgical Transactions A. 9 (1978) 101-110.

[46] R.C. Lobb, R.B. Jones, Creep-rupture properties of fecralloy stainless steel between 650 and 800 ^{0}C, J. Nucl. Mater. 91 (1980) 257-264.

[47] K.G. Field, M.A. Snead, Y. Yamamoto, K.A. Terrani, Handbook on the Material Properties of FeCrAl Alloys for Nuclear Power Production Applications, Nuclear Technology Research and Development. (2017).

[48] M.N. Gussev, T.S. Byun, Y. Yamamoto, S.A. Maloy, K.A. Terrani, In-situ tube burst testing and high-temperature deformation behavior of candidate materials for accident tolerant fuel cladding, J. Nucl. Mater. 466 (2015) 417-425.

[49] K.A. Terrani, T.M. Karlsen, Y. Yamamoto, Input correlations for irradiation creep of FeCrAl and SiC based on in-pile Halden test results, Oak Ridge National Laboratory (ORNL), Oak Ridge, TN (United States). (2016).

[50] S. Saunders, H.E. Evans, M. Li, D.D. Gohil, S. Osgerby, Oxidation growth stresses in an alumina-forming ferritic steel measured by creep deflection, Oxidation Metals. 48 (1997) 189-200.

[51] P. Seiler, M. Bäker, J. Rösler, Influence of creep and cyclic oxidation in thermal barrier coatings, International Journal of Materials Research. 103 (2012) 50-56.

[52] R.J. Beauregard, G.S. Clevinger, K.L. Murty, Effect of annealing temperature on the mechanical properties of Zircaloy-4 cladding, Structural Mechanics in Reactor Technology, 1977.

[53] F.C. Monkman, An empirical relationship between rupture life and minimum creep rate in creep rupture tests, 56 (1956) 91-103.

[54] RL Klueh, The relationship between rupture life and creep properties of 2 1/4 Cr-1 Mo steel, osti.gov, 1974

[55] F.R. Larson, A time-temperature relationship for rupture and creep stresses, Trans.ASME. 74 (1952) 765-775.

[56] C.J. Smithells, E.A. Brandes, Smithells Metals Reference Book, 1992.

[57] G. Srikant, B. Marple, I. Charit, K.L. Murty, Characterization of stress rupture behavior of commercial-purity-Ti via burst testing, Materials Science and Engineering: A. 463 (2007) 203-207.

[58] Shanghai EverSkill M&E Co., Ltd, http://www.esmeind.com/Pro-Tube.html, 2018.

[59] Cold Pilger Rolling: Part One, http://www.totalmateria.com/page.aspx?ID=CheckArticle&site=kts&NM=396, (2013).